Electronic Structure Studies of Main Group Oxides Possessing Edge-Sharing Octahedra: Implications for the Design of Transparent Conducting Oxides

Hiroshi Mizoguchi and Patrick M. Woodward*

Department of Chemistry, The Ohio State University, Columbus, Ohio 43210-1185

Received May 13, 2004. Revised Manuscript Received August 20, 2004

Experimental and computational studies were performed to investigate the electronic structure of main group oxides containing edge-sharing octahedra. Compounds belonging to four structure types were investigated: rutile (SnO_2, PbO_2), trirutile ($MgSb_2O_6$, $ZnSb_2O_6$, $MgBi_2O_6$, $ZnBi_2O_6$), $PbSb_2O_6$-type ($CdSb_2O_6$, $CaSb_2O_6$, $SrSb_2O_6$, $BaSb_2O_6$, $SrBi_2O_6$, $BaBi_2O_6$), and ilmenite ($ZnSnO_3$, $CdSnO_3$, $CaSnO_3$, $NaSbO_3$, $KSbO_3$, $NaBiO_3$, $AgBiO_3$). For application as an *n*-type transparent conductor, the conduction band (CB) properties are of primary importance. In all compounds investigated here, the CB arises primarily from the antibonding *M n*s to O 2p interaction (*M* = Sn, Pb, Sb, Bi). To be an effective transparent conductor the lowest energy band in the CB should be wide so that carriers introduced upon doping will be highly mobile. For this to occur, the antibonding *M n*s to O 2p interactions must be offset by a bonding interaction at the CB minimum (normally at the Γ point). In ternary oxides, the bonding interaction involves overlap between the empty valence shell s orbital on the charge compensating *A* cation (*A* = Mg^{2+}, Ca^{2+}, Sr^{2+}, Ba^{2+}, Na^{+}, K^{+}, Ag^{+}, Cd^{2+}, Zn^{2+}) with unfilled antibonding states originating on the edge-sharing octahedral framework. A disperse CB is obtained when the electronegativity of the *A* cation is such that it enables a covalent interaction with oxygen, and the oxygen coordination environment is symmetric. These conditions are met in $ZnSb_2O_6$ (trirutile), $CdSb_2O_6$ ($PbSb_2O_6$-type), $CdSnO_3$ (ilmenite), $ZnSnO_3$ (ilmenite), and $AgBiO_3$ (ilmenite), as well as the binary oxides SnO_2 and In_2O_3 (corundum polymorph). When *M* is Bi^{5+} or Pb^{4+}, relativistic effects reduce the spatial overlap between *M* 6s orbital and the oxygen orbitals. This effect lowers the energy of the conduction band, thereby narrowing the band gap. Consequently, in these materials, it is generally not possible to simultaneously obtain a disperse CB and a wide band gap, limiting applications as transparent conductors.

1. Introduction

Transparent conducting oxides (TCOs) are used in a wide variety of applications including flat panel displays, energy-efficient window coatings, photovoltaics, organic and inorganic light emitting diodes, and antistatic coatings. The materials that are best known and most extensively studied for this behavior are *n*-doped binary metal oxides, such as In_2O_3, ZnO, CdO, and SnO_2. Fluorine-doped SnO_2 is the most widely utilized material for energy-efficient window coatings, while $(In_{1-x}Sn_x)_2O_3$ (ITO) dominates the market for flat panel displays, a market that is projected to grow to over $27 billion per annum by the year 2005.[1] As TCO materials are used increasingly in thin film devices, the relative scarcity of effective TCO materials becomes problematic, due to the fact that the device efficiency depends in part on the lattice and energy level matching between the TCO and the active material upon which TCO layer is to be deposited. Cost, stability in harsh environments, ease of film deposition, responsiveness to chemical etching, and chemical compatibility with neighboring layers are also important design criteria. With these considerations in mind, it is not possible for one or two materials to be optimal for all applications. This provides a strong incentive to search for new TCO materials.

Despite the widespread applications of TCOs, the structural and compositional features that are favorable for transparent conductivity are not fully understood. It is widely accepted that *n*-type TCO materials should contain a metal with a $(n-1)d^{10}ns^0$ electronic configuration. Among the binary oxides, In_2O_3, SnO_2, CdO, ZnO, and Ga_2O_3 are well-known to be transparent conductors. There has been much less attention paid to ternary and quaternary oxides, but if new TCO materials are to be found, it is necessary to investigate complex oxides. To the best of our knowledge, the first report of a ternary TCO was a study of Cd_2SnO_4, by Nozik and later Haacke and co-workers in 1970s.[2,3] Shannon et al. expanded the list of ternary TCOs to include $CdSnO_3$, Cd_2SnO_4, In_2TeO_6, and $CdIn_2O_4$ in 1977.[4] In that paper,

* To whom correspondence should be addressed. E-mail: woodward@chemistry.ohio-state.edu.

(1) Ginley, D. S.; Bright, C. *Mater. Res. Soc. Bull.* **2000**, *25*, 15 (August).

(2) Nozik, A. J. *Phys. Rev. B* **1972**, *6*, 453.

(3) (a) Haacke, G. *Appl. Phys. Lett.* **1976**, 28, 622. (b) Haacke, G.; Ando, H.; Mealmaker, W. E. *J. Electrochem. Soc.* **1977**, *124*, 1923.

10.1021/cm049249w CCC: $27.50
Published on Web 11/13/2004

they speculate that continuous edge sharing of Cd^{2+}, In^{3+}, and Sn^{4+} octahedra may be a necessary criterion for the formation of a transparent conductor. Following these early studies, a number of research groups has studied complex oxides as TCO materials.[5,6,7,8] Nearly all of the complex TCOs found to date possess cations in octahedral coordination, as do most binary TCOs, with the exception of ZnO (wurtzite structure) and β-Ga_2O_3 (Ga^{3+} ions are split equally over octahedral and tetrahedral sites). These and other studies show that complex oxides may be a rich source of new TCO materials, but there are a number of unanswered questions. For example, why is octahedral coordination about the cation such a dominant feature and what is special about ZnO, where all of the cations are tetrahedrally coordinated? Is there any reason to favor structures possessing edge-sharing octahedra over those possessing corner-sharing octahedra? Is TCO behavior limited to compounds where all of the cations have $(n - 1)d^{10}ns^0$ configuration, or can electronically inert cations (alkali, alkaline earth, and/or rare-earth cations) be effectively used in the design of TCO materials? In an earlier paper, we considered the electronic structures of perovskites and pyrochlores (both structures possessing corner-sharing octahedral topologies) containing Sn^{4+} and Sb^{5+}.[9] In this paper, we investigate the electronic properties of ternary oxides containing Sn^{4+}, Sb^{5+}, or Bi^{5+}, focusing on structures containing two- or three-dimensional networks of edge sharing octahedra, namely, the rutile, trirutile, $PbSb_2O_6$, and ilmenite structure types. The combined results of the two studies allow us to draw some conclusions about the structural and compositional features that are favorable for the occurrence of transparent conductivity.

2. Experimental Procedures

Samples of SnO_2 (99.9%, Fisher), PbO_2 (95%, EM Science), and $NaBiO_3$ (99.9%, Aldrich) were purchased. The phase purity of these samples was confirmed by powder X-ray diffraction. $NaBiO_3$ was heated at 520 K for 1 h to remove crystal water.[10] Samples of $ZnSb_2O_6$,[11] $SrSb_2O_6$,[12] $BaSb_2O_6$, [12] $CdSb_2O_6$,[13] $NaSbO_3$,[14] and $KSbO_3$[15] were synthesized by solid-state reaction at elevated temperatures. SnO_2 (99.9%, Fisher), ZnO (99.9%, Mallinckrodt), Sb_2O_3 (99.9%, Cerac), $SrCO_3$ (99.9+%, Aldrich), $BaCO_3$ (99.4%, Mallinckrodt), $Cd(NO_3)_2{\cdot}4H_2O$ (Mallinckrodt), $NaNO_3$ (Jenneile), and K_2CO_3 (99% minimum, Fisher) were used as reagents. $Cd(NO_3)_2{\cdot}4H_2O$ was heated at 770 K for 1 h to convert into CdO, before weighing. These reagents were mixed in an alumina mortar and pestle with ethanol. For synthesis of $ZnSb_2O_6$, the starting materials were first prefired at 1170 K for 4 h. After the prefiring step, the obtained products were ground, pelletized, and heated at 1270 K for 4 h in air. $SrSb_2O_6$ and $BaSb_2O_6$ were prepared by heating at 1270 K for 10 h in air without prefiring. Several heating stages were used to prepare $CdSb_2O_6$. The mixed reagents were ground, pelletized, and heated in air at 850 K for 24 h, 1170 K for 24 h, 1220 K for 12 h, and 1270 K for 48 h. The ilmenites $NaSbO_3$ and $KSbO_3$ were prepared directly by heating in air without a prefiring step, $NaSbO_3$ at 1270 K for 5 h and $KSbO_3$ at 1070 K for 12 h. For $KSbO_3$, all steps were performed quickly to limit the amount of moisture absorption from the air, which induces the formation of the cubic polymorph of $KSbO_3$.

Wet chemical methods starting from an Sb_2O_5 sol[16] were utilized for the synthesis of $MgSb_2O_6$ and $CaSb_2O_6$. Sb_2O_3 (0.8 g, 99.9%, Cerac) and H_2O_2 (20 mL) were added to water (100 mL). The suspension was stirred for 1 h at 360 K. An aqueous solution of stoichiometric $MgCl_2{\cdot}6H_2O$ (99%, EM Science) or $Ca(NO_3)_2{\cdot}4H_2O$ (99.0%, Mallinckrodt) was poured slowly into the antimony oxide sol, and the mixture was heated until evaporation of the solvent was achieved. After drying, the samples were pressed into pellets and heated to 1320 K for 4 h for $MgSb_2O_6$ or 1270 K for 10 h for $CaSb_2O_6$, respectively.

ABi_2O_6 (A = Zn^{2+},[17] Mg^{2+},[17] Sr^{2+}, Ba^{2+}) and $AgBiO_3$[10] samples were synthesized by hydrothermal methods. In each case, $NaBiO_3$ was reacted with an appropriate source of the A-site cation, $Zn(NO_3)_2{\cdot}6H_2O$ (99%, Matheson, Coleman and Bell) for $ZnBi_2O_6$, $MgCl_2{\cdot}6H_2O$ for $MgBi_2O_6$, $SrCl_2{\cdot}6H_2O$ (J. T. Baker) for $SrBi_2O_6$, $BaCl_2{\cdot}2H_2O$ (Mallinckrodt) for $BaBi_2O_6$, and $AgNO_3$ (99.9+%, Alfa Aesar) for $AgBiO_3$. Both reagents were placed with water in a Teflon lined autoclave and kept at 390, 370, 360, 410, and 360 K, respectively, for 48 h. The obtained powders were filtered and washed twice with water and once with acetone, then dried at 320 K in air.

Single-phase samples of $CdSnO_3$ in its ilmenite form were difficult to prepare by conventional solid-state reaction. Invariably, the perovskite polymorph of $CdSnO_3$ was formed in addition to the desired ilmenite phase. To overcome this obstacle, we prepared $CdSnO_3$[18] in its ilemnite form by ion exchange of Li_2SnO_3 in a $CdCl_2$ (68 mol %)/KCl(32 mol %) flux in a Pt crucible at 870 K for 50 h under flowing argon. The obtained powder was washed with dilute HNO_3 to remove the residual impurity phase, Cd_2SnO_4. The Li_2SnO_3 precursor was synthesized by solid-state synthesis, by reacting Li_2CO_3 (99.997%, Aldrich) and SnO_2 at 820 K for 50 h with several intermediate grindings. $CdCl_2$ was prepared by adding CdO to a dilute HCl aqueous solution at 360 K and evaporating the solvent. $ZnSnO_3$[19] and $CaSnO_3$ in its ilmenite form[20] were also synthesized by ion exchange from a Li_2SnO_3 host using $ZnCl_2$ (50 mol %)/KCl (50 mol %) and $CaCl_2$ (47 mol %)/NaCl (53 mol %) fluxes, respectively. For $ZnSnO_3$, the reaction was performed in quartz tube in air at 620 K for 20 h. For $CaSnO_3$ the reaction was performed in Pt crucible in the flow of N_2 gas at 820 K for 50 h. In the latter case, the reaction under argon gas flow did not lead to the formation of a single-phase product. KCl (99.9%, Fisher), $ZnCl_2$ (99.9%, Alfa Aesar), $CaCl_2{\cdot}2H_2O$ (J. T. Baker), and NaCl (99.9%, Fisher) reagents were used during the ion exchange step. To prepare samples of In_2O_3 in its corundum form, high-pressure synthesis is normally required.[21,22] To overcome this obstacle, we prepared In_2O_3 by thermal decomposition of $NaInO_2$ (0.5 g) in a $Ca(NO_3)_2{\cdot}4H_2O$ (40 mol %)/$NaNO_3$ (60 mol %) flux (5.7 g) in a quartz tube at 600 K for 48 h under air. The obtained powder was washed

(4) Shannon, R. D.; Gilson, J. L.; Bouchard, R. J. *J. Phys. Chem. Solids* **1977**, *38*, 877.
(5) Kawazoe, H.; Ueda, N.; Un'no, H.; Omata, T.; Hosono, H.; Tanoue, H. *J. Appl. Phys.* **1994**, *76*, 7935.
(6) Cava, R. J.; Phillips, J. M.; Kwo, J.; Thomas, G. A.; van Dover, R. B.; Carter, S. A.; Krajewski, J. J.; Peck, W. F., Jr.; Marshall, J. H.; Rapkine, D. H. *Appl. Phys. Lett.* **1994**, *64*, 2071.
(7) Minami, T. *Mater. Res. Soc. Bull.* **2000**, *25*, 38 (August).
(8) Freeman, A. J.; Poeppelmeier, K. R.; Mason, T. O.; Chang, R. P. H.; Marks, T. J. *Mater. Res. Soc. Bull.* **2000**, *25*, 45 (August).
(9) Mizoguchi, H.; Eng, H. W.; Woodward, P. M. *Inorg. Chem.* **2004**, *43*, 1667.
(10) Kumada, N.; Kinomura, N.; Sleight, A. W. *Mater. Res. Bull.* **2000**, *35*, 2397.
(11) Nishiyama, K.; Hattori, H. *J. Ceram. Soc. Jpn.* **2000**, *108*, 435.
(12) DeBoer, B. G.; Young, R. A.; Sakthivel, A. *Acta Crystallogr., Sect. C* **1994**, *50*, 476.
(13) Yanagawa, K.; Ohki, Y.; Omata, T.; Hosono, H.; Ueda, N.; Kawazoe, H. *Appl. Phys. Lett.* **1994**, *65*, 406.
(14) Wang, B.; Chen, S. C.; Greenblatt, M. *J. Solid State Chem.* **1994**, *108*, 184.
(15) Spiegenberg, P. *Ark. Kemi. Mineral. Geol. A* **1940**, *14*, 1.
(16) Brisse, F.; Stewart, D. J.; Seidl, V.; Knop, O. *Can. J. Chem.* **1972**, *50*, 3648.
(17) Kumada, N.; Takahashi, N.; Kinomura, N.; Sleight, A. W. *Mater. Res. Bull.* **1997**, *32*, 1003.
(18) Morgenstern-Badarau, I.; Poix, U. P.; Michel, A. *Compt. Rend. Acad. Sci.* **1964**, *258*, 3036.
(19) Kovacheva, D.; Petrov, K. *Solid State Ionics* **1998**, *109*, 327.
(20) Durand, B. *J. Appl. Crystallogr.* **1978**, *11*, 289.
(21) Prewitt, C. T.; Shannon, R. D.; Rogers, D. B.; Sleight, A. W. *Inorg. Chem.* **1969**, *8*, 1985.

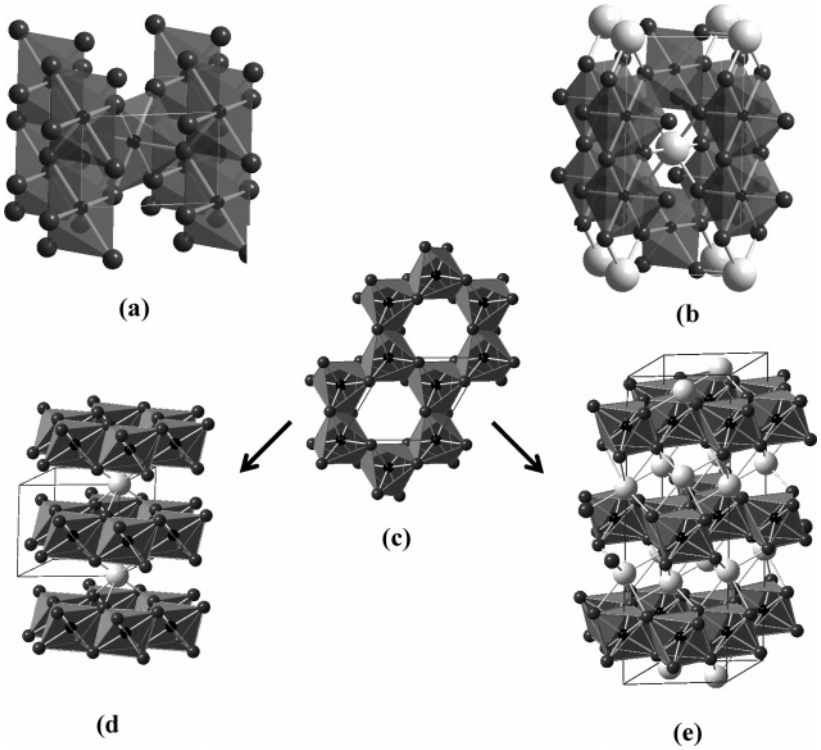

Figure 1. Crystal structures of (a) the rutile structure (SnO_2), (b) the trirutile structure ($MgBi_2O_6$), (c) the $Sb_2O_6^{2-}$ layers common to the $PbSb_2O_6$ and ilmenite structure types, (d) the $PbSb_2O_6$-type structure ($CdSb_2O_6$), and (e) the ilmenite structure ($NaBiO_3$). The *A* cations (Mg^{2+}, Cd^{2+}, Na^+) are shown as larger light gray spheres, the *M* cations are shown as smaller black spheres within the octahedra, and the oxide ions are shown as smaller spheres at the vertices of the octahedra.

with water followed by 2 M HNO_3 to remove the residual impurity phase. The $NaInO_2$ precursor with $(InO_2)^-$ layers was synthesized by solid-state synthesis, by reacting excess Na_2CO_3 and In_2O_3 at 1120 K for 24 h with an intermediate grinding. We believe that the ion exchange between Na^+ in $NaInO_2$ and cationic species in the molten salts at low temperature induces the decomposition of $NaInO_2$, which in turn induces a structural rearrangement from the layered structure to In_2O_3 with the corundum structure. Na_2CO_3 (99.5%, Fisher) and In_2O_3 (99.99%, Cerac) reagents were used.

Cation stoichiometries for all compounds synthesized were confirmed by X-ray energy dispersive spectroscopy using a SEM (JEOL, JSM-820 with Oxford eXL analyzer). Phase purity was checked, and structure analysis was carried out using laboratory X-ray powder diffraction (XRPD). XRPD data was collected in Bragg−Brentano mode using a Bruker D8 X-ray powder diffractometer (40 kV and 50 mA, sealed Cu X-ray tube) equipped with an incident beam Ge 111 monochromator, which selects only $CuK\alpha_1$ radiation, and a Braun linear position sensitive detector. Structure refinements were performed using the Rietveld method[23] as implemented in the TOPAS software package.[24]

UV−vis diffuse reflectance data was collected over the spectral range 240−1100 nm using a Perkin-Elmer Lambda 20 scanning double-beam spectrometer, equipped with a 50 mm Labsphere integrating sphere. In instances where absorbance data were needed further into the IR region, a Perkin-Elmer Lambda 900 double beam spectrometer was used to access the spectral range 1100−2600 nm. MgO was used as a reference. The data were transformed into absorbance using the Kubelka−Munk function.

Band structure calculations were performed using the linear muffin-tin orbital (LMTO) method with the atomic sphere approximation (ASA) including the combined correction (CC). The LMTO-ASA code used in these calculations was developed in Stuttgart by Andersen and co-workers.[25] Intersitial space was filled with empty spheres. *k*-Space integrations employed the tetrahedron method using irreducible *k* points within the Brillouin zone (BZ). The number of *k* points included in the calculation was 252 for SnO_2, 84 for the trirutile structure, 131 for the $PbSb_2O_6$-type structure, 294 for the ilmenite structure, and 189 for corundum structure. The basis sets consisted of the valence s, p, and d orbitals of cations and the 2s and 2p orbitals of oxygen. The Perdew−Wang generalized gradient approximation was used to treat the effects of exchange and correlation.[26] Extended Huckel tight binding (EHTB) calculations were also performed to elucidate the bonding interactions that play a strong role near the Fermi energy. The EHTB calculations were carried out using the commercially available software program, CAESAR.[27] In the case of the ilmenite and corundum compounds, the calculations were done on the rhombohedral unit cell ($A_2M_2O_6$ or M_4O_6) to minimize computational time.

3. Results and Discussion

3.1 Structure Description and Analysis. Both SnO_2 and β-PbO_2 adopt the rutile structure as shown in Figure 1a. Detailed structure determinations have been previously carried out and reported in the literature.[28] The metal cation, *M*, is surrounded by six oxygen anions in a slightly distorted octahedron, while the

(22) (a) Frank, G.; Olazcuaga, R.; Rabenau, A. *Inorg. Chem.* **1976**, *16*, 1251. (b) Hernan, L.; Macias, M.; Morales, J. *Mater. Res. Bull.* **1990**, *25,* 1169. (c) Yu, D.; Wang, D.; Lu, J.; Qian, Y. *Inorg. Chem. Commun.* **2002**, *5*, 475. (d) Epifani, M.; Siciliano, P.; Gurlo, A.; Barsan, N.; Weimer, U. *J. Am. Chem. Soc.* **2004**, *126*, 4078.

(23) Young, R. A. *The Rietveld Method*; Oxford Press: London, 1995.

(24) Cheary, R. W.; Coelho, A. A. *J. Appl. Crystallogr.* **1992**, *25*, 109.

(25) Andersen, O. K.; Pawlowska, Z.; Jepsen, O. *Phys. Rev. B* **1986**, *34*, 5253.

(26) Perdew, J. P.; Wang, Y. *Phys. Rev. B* **1986**, *33*, 8800.

(27) Ren, J.; Liang. W.; Whangbo, M.-H. PrimeColor Software Raleigh, 1998; http://www.PrimeC.com/

(28) Bolzan, A. A.; Fong. C.; Kennedy, B. J.; Howard, C. J. *Acta Crystallogr., Sect. B* **1997**, *53*, 373.

Table 1. Crystal Structure of $MgSb_2O_6$, as Determined from Analysis of a Monochromatic CuKα_1 X-ray Diffraction Data Set Covering the 2θ Range 10−130°[a]

atom	Wyckoff site	x	y	z	occupation factor	B_{iso} (Å^2)[b]
Mg	2a	0	0	0	0.940(3)	0.001(1)
Sb	2a	0	0	0	0.060(3)	0.001(1)
Mg	4e	0	0	0.33228(8)	0.030(1)	0.0015(1)
Sb	4e	0	0	0.33228(8)	0.970(1)	0.0015(1)
O(1)	4f	0.306(1)	0.306(1)	0	1	0.0007(7)
O(2)	8j	0.3041(7)	0.3041(7)	0.3273(7)	1	0.0007(7)

[a] The Rietveld refinement ($R_{wp} = 16.20\%$, $R_{Bragg} = 2.74\%$, $\chi^2 = 1.88$) was carried out using space group $P4_2/mnm$ with unit cell parameters of $a = 4.64844(4)$ and $c = 9.2291(1)$. [b] The displacement parameters for the O(1) and O(2) sites were constrained to be equal.

Table 2. Structural Features of Rutile and Trirutile Main Group Oxides

compound	$M-O$ distances (Å)	$M-M$ distance (Å)	O(1)−A/M distances (Å)	O(2)−A/M distances (Å)	M−O−M angles (deg)	M−O−A angles (deg)
SnO_2[28]	2 × 2.048	3.187	2 × 2.058 (Sn)		101.5	
	4 × 2.058		1 × 2.048 (Sn)			
PbO_2[28]	2 × 2.154	3.388	2 × 2.167 (Pb)		102.8	
	4 × 2.167		1 × 2.154 (Pb)			
$MgSb_2O_6$	2 × 1.956(5)	3.096	2 × 2.006(3) (Sb)	1.956(5) (Sb)	101.0	99.9(2)
	2 × 2.000(4)		1 × 2.012(5) (Mg)	2.000(4) (Sb)		
	2 × 2.006(3)			2.050(6) (Mg)		
$ZnSb_2O_6$[29]	2 × 1.974	3.086	2 × 2.004 (Sb)	1.974 (Sb)	100.7	99.6
	2 × 1.997		1 × 2.017 (Zn)	1.997 (Sb)		
	2 × 2.004			2.052 (Zn)		
$MgBi_2O_6$[17]	2 × 2.090	3.266	2 × 2.106 (Bi)	2.075 (Mg)	101.6	101.5
	2 × 2.095		1 × 2.082 (Mg)	2.090 (Bi)		
	2 × 2.106			2.095 (Bi)		

oxygen is coordinated by three metal cations in a planar geometry where the bond angles are somewhat distorted from 120°. The site symmetry of the oxygen site is C_{2v}, and that of the M site is D_{2h}. The rutile structure contains infinite linear chains of edge-sharing MO_6 octahedra running parallel to the c-axis. Across the shared edge the $M-M$ distance is 3.19 Å in SnO_2 and 3.39 Å in PbO_2. By comparison, the $M-M$ distances are 2.81 and 3.50 Å in the elemental forms of tin (α) and lead. Despite the relatively long Sn−Sn distance, it is sometimes suggested that direct overlap of Sn 5s orbitals across the shared octahedral edge plays an important role in the electronic properties of n-doped SnO_2. Regardless of the importance of the Sn−Sn interactions, it is incorrect to think of the rutile structure as a 1-D or even a psuedo-1-D structure. Each chain is connected to four neighboring chains, each shifted by one-half unit cell along the c-axis. This produces a structure where each oxygen ion acts as bridging ligand across the shared edge of one chain, while at the same time axially coordinating to a cation in a neighboring chain.

The trirutile structure, shown in Figure 1b, typically has AM_2O_6 stoichiometry and is an ordered variant of rutile. Most commonly, A is a divalent ion and M is a pentavalent ion. The trirutile structure adopts the same space group symmetry as rutile ($P4_2/mnm$), but the c-axis of the unit cell is tripled. The need to triple the c-axis is evident from the $A-M-M-A-M-M-$... cation sequence observed within each rutile chain. There are now two crystallographic sites for oxygen, but the chemical environments of the two sites are similar. Each oxygen is coordinated to two M cations and one A cation, and the planar coordination environment is retained. Inclusion of trirutile compounds allows us to extend our investigation to oxides of Sb^{5+} and Bi^{5+}, by including $MgSb_2O_6$, $ZnSb_2O_6$, $MgBi_2O_6$, and $ZnBi_2O_6$. The crystal structures of $ZnSb_2O_6$[29] and $MgBi_2O_6$[17] have been previously reported, whereas detailed structural data is not available for $MgSb_2O_6$ and $ZnBi_2O_6$. This prompted us to carry out Rietveld refinements of their structures from X-ray powder diffraction data. The results of this analysis for $MgSb_2O_6$ are given in Table 1, while the observed, calculated, and difference patterns are shown in the Supporting Information. The refinements suggest that a small degree of cation disorder is present. This finding is consistent with the observations made by Horiuchi et al. using transmission electron diffraction.[30] The structure of $ZnBi_2O_6$ was also refined. The unit cell dimensions were determined to be $a = 4.84135(6)$ Å and $c = 9.7506(2)$ Å. These values are in good agreement with the values previously reported ($a = 4.839$ Å and $c = 9.742$ Å) and not significantly different from those reported for $MgBi_2O_6$ ($a = 4.826$ Å and $c = 9.719$ Å).[17] Unfortunately, the presence of bismuth makes it difficult to determine the oxygen positions with sufficient accuracy to merit a valid comparison with the other compounds in this series. From the similarity of the lattice parameters, it is reasonable to assume that the bond distances and angles in $ZnBi_2O_6$ are very similar to those previously reported for $MgBi_2O_6$. Select bond distances and angles are listed in Table 2 for the rutile and trirutile compounds studied here. Comparison of $MgSb_2O_6$ and $ZnSb_2O_6$ shows that the environment about Sb^{5+} is relatively insensitive to substitution on the A-site. From the lattice parameter comparison, we infer a similar scenario for $MgBi_2O_6$ and $ZnBi_2O_6$. The apparent rigidity of the M_2O_6 network is responsible for the relatively small region of stability of the trirutile structure. We will see below that increasing the radius

(29) Bystroem, A.; Hoek, B.; Mason, B. *Ark. Kemi. Mineral. Geol. B* **1942**, *15*, 1.
(30) Horiuchi, S.; Uchida, K.; Kikuchi, T. *Trans. Jpn. Inst. Metals* **1983**, *24*, 443.

Table 3. Crystal Structure of $CdSb_2O_6$, as Determined from Analysis of a Monochromatic $CuK\alpha_1$ X-ray Diffraction Data Set Covering the 2θ Range 15−120°[a]

atom	Wyckoff site	x	y	z	B_{iso} (Å^2)
Cd	1a	0	0	0	0.0036(3)
Sb	2d	1/3	2/3	1/2	0.0003(2)
O	6k	0.365(1)	0	0.282(1)	0.005(2)

[a] The Rietveld refinement (R_{wp} = 18.4%, R_{Bragg} = 4.06%, χ^2 = 2.03) was carried out using space group $P\bar{3}1m$ with unit cell parameters of a = 5.23726(5) and c = 4.79826(8).

of the *A*-site cation destabilizes the rutile structure in favor of the $PbSb_2O_6$ structure type.

The second set of compounds that were investigated adopt the $PbSb_2O_6$ structure type (space group = $P\bar{3}1m$), with AM_2O_6 stoichiometry. The $PbSb_2O_6$ structure contains two-dimensional layers of edge-sharing SbO_6 octahedra, where two out of every three octahedral holes are filled as shown in Figure 1c. Because of the large positive valence of the *M*-site cation, the bonding within this layer is fairly covalent. The Pb^{2+} ions occupy one out of every three octahedral holes in adjoining layers. The Pb^{2+} ions fill the octahedral holes that sit immediately above and below the vacant octahedral site in the Sb_2O_6 layers; see Figure 1d. The *A*−O interaction is generally fairly ionic. Thus, the electronic structure and physical properties of these compounds are expected to be pseudo-two-dimensional. Oxygen sits on the *6k* Wyckoff site with C_s symmetry. Each oxygen anion is coordinated by two *M*-site and one *A*-site cations in a geometry that is slightly distorted from trigonal planar. The structures of the ASb_2O_6-type oxides (*A* = Cd, Ca, Sr, Ba) have been previously determined.[12,31] However, the reported crystal structure of $CdSb_2O_6$[31] has rather short Cd−O distances (6 × 2.185 Å), which led us to reinvestigate its structure. Our analysis gives a more realistic value of 2.344(7) Å for the Cd−O distance (by way of comparison the Cd−O distance in CdO is 2.35 Å).[32] The refined structure is given in Table 3, while the observed, calculated, and difference patterns are shown in the Supporting Information. Select bond distances and angles for ASb_2O_6 compounds are listed in Table 4.

Kumada et al. reported the systematic synthesis of several new oxides using $NaBiO_3$ as a starting material. Small *A*-site cations, such as Mg and Zn, generate compounds with the trirutile structure as already discussed,[17] whereas large *A*-site cations, such as Sr and Ba, yielded either compounds where the trigonal Bi_2O_6 layers appear to be retained,[33] or compounds that adopt the defect pyrochlore structure.[34] With the larger alkaline-earth cations (Ca, Sr, Ba), either it was not possible to fully displace the sodium (layered compounds), or polyatomic anions, such as carbonate and hydroxide, were retained (defect pyrochlores). The compound $LiBiO_3$, which adopts a unique structure type, has also been prepared through ion exchange starting from $NaBiO_3$.[35] Using hydrothermal methods, we were able to successfully synthesize the compounds $SrBi_2O_6$ and $BaBi_2O_6$ for the first time. The XRPD patterns of these two phases, which are shown in the Supporting Information, could be indexed using a hexagonal unit cell with unit cell dimensions and systematic absences consistent with the $PbSb_2O_6$ structure type. Previously, Kumada et al. prepared hexagonal phases with compositions $A_xNa_{1-2x}BiO_3{\cdot}nH_2O$ (*A* = Sr, Ba),[33] so the fact that we were able to index the XRPD patterns using a hexagonal cell does not prove that our samples have the target stoichiometry. However, there are several additional pieces of evidence that support this assertion. EDS analysis gives *A*/Bi ratios of 1:2 for both $SrBi_2O_6$ and $BaBi_2O_6$. The occupancies of the *A*-sites were also estimated from XRPD, via Rietveld refinements, to be 1:2 for $SrBi_2O_6$ and 1:2 for $BaBi_2O_6$. Thermogravimetric analysis (TGA) shows a mass loss near 470 K, suggesting some water of hydration is present. This conclusion is supported by the fact that neutron powder diffraction data sets for both compounds possessed very high background levels, indicating that significant concentrations of hydrogen are present. Using the TGA data to estimate the water content gives stoichiometries of $SrBi_2O_6{\cdot}0.51H_2O$ and $BaBi_2O_6{\cdot}0.32H_2O$. As was the case with $ZnBi_2O_6$, the XRPD refinements did not provide oxygen coordinates that were sufficiently accurate to allow meaningful comparison with the ASb_2O_6 phases. The X-ray patterns also show anisotropic peak broadening suggesting either the presence of stacking faults or the formation of crystals with very anisotropic dimensions.

The third set of compounds that were investigated in this study adopt the ilmenite structure (space group = $R\bar{3}$), with stoichiometry AMO_3. This structure is closely related to the $PbSb_2O_6$ structure as illustrated in Figure 1e. The ilmenite structure contains M_2O_6 layers that have the same topology as the Sb_2O_6 layers in $PbSb_2O_6$. However, the stoichiometry dictates that twice as many *A*-site cations must be accommodated in the octahedral holes between the M_2O_6 layers. Consequently, each *A*-site cation shares one face of its octahedron with a MO_6 octahedron in the neighboring layer. The electrostatic repulsion between cations causes the *A*- and *M*-site cations to shift away from each other. Each cation shifts toward an octahedral face that is shared with a vacant octahedral hole. The cation displacement from the center of its coordination polyhedron increases as the ionicity of the cation−anion bond increases. The ilmenite structure can also be described as an ordered corundum structure, where the *c*-glide plane in corundum is destroyed by imposition of a layered ordering of the cations. The oxygen atoms in ilmenite are four coordinate. The geometry can loosely be described as a highly distorted tetrahedron. The *M*−O−*M* angles and *M*−O distances are observed to be similar to the rutile, trirutile, and $PbSb_2O_6$ compounds already discussed. The crystal structures of several stannate antimonate and bismuthate ilmenites of interest have previously been determined, with the exception of $CdSnO_3$. Therefore, we collected XRPD data and applied the Rietveld method to determine the crystal structure of the ilmenite polymorph of $CdSnO_3$. The refinement results are summarized in Table 5, while the observed, calculated, and difference patterns are shown in the Sup-

(31) Castro, A.; Rosines, I.; Sanchez-Martos, M. C.; Garcia-Casado, P. *Powder Diffraction* **1988**, *3*, 219.
(32) Cimino, A.; Marezio, M. *J. Phys. Chem. Solids* **1960**, *17*, 57.
(33) Kumada, N.; Kinomura, N.; Sleight, A. W. *Solid State Ionics* **1999**, *122*, 183.
(34) Kumada, N.; Hosoda, M.; Kinomura, N. *J. Solid State Chem.* **1993**, *106*, 476.
(35) Kumada, N.; Takahashi, N.; Kinomura, N.; Sleight, A. W. *J. Solid State Chem.* **1996**, *126*, 121.

Table 4. Structural Features of $PbSb_2O_6$-Type Oxides, ASb_2O_6

compound	$M-O$ distances (Å)	$M-M$ distances (Å)	$O-A/M$ distances (Å)	$M-O-M$ angles (deg)	$M-O-A$ angles (deg)
$CaSb_2O_6$[12]	6 × 1.961	3.025	2 × 1.961 (Sb) 1 × 2.437 (Ca)	101.0	126.4
$SrSb_2O_6$[12]	6 × 1.957	3.044	2 × 1.957 (Sb) 1 × 2.58 (Sr)	102.1	126.2
$BaSb_2O_6$[12]	6 × 1.956	3.062	2 × 1.956 (Sb) 1 × 2.745 (Ba)	103.0	126.0
$CdSb_2O_6$	6 × 1.969(4)	3.023	2 × 1.969 (Sb) 1 × 2.344 (Cd)	100.6	126.9

Table 5. Crystal Structure of the Ilmenite Polymorph of $CdSnO_3$, as Determined from Analysis of a Monochromatic CuKα$_1$ X-ray Diffraction Data Set Covering the 2θ Range 10−120°[a]

atom	Wyckoff site	x	y	z	B_{iso} (Å^2)
Cd	2c	0.3660(1)	0.3660(1)	0.3660(1)	0.010(1)
Sn	2c	0.1544(1)	0.1544(1)	0.1544(1)	0.010(1)
O	6f	0.571(2)	0.962(2)	0.214(2)	0.011(1)

[a] The Rietveld refinement (R_{wp}=13.8%, R_{Bragg}=7.08%, χ^2 =1.75) was carried out using space group $R\bar{3}$ with unit cell parameters of a = 5.9005(2) and α = 55.058(2).

porting Information. Select bond distances and angles for a number of $ASnO_3$, $ASbO_3$, and $ABiO_3$ ilmenites are listed in Table 6. Included in this list for comparison is the high-pressure phase of In_2O_3, which adopts the corundum structure.[21]

When the A and M cations have similar ionic radii and electronegativities, as is the case for $ZnSnO_3$ and $CdSnO_3$, the ilmenite structure can be considered similar to corundum with a periodic cation ordering imposed. The electronic structure and physical properties of these compounds should be three-dimensional in nature. On the other hand, when the A-site cation is large and electropositive, as is the case for $NaSbO_3$, $KSbO_3$, $NaBiO_3$, and $CaSnO_3$, it is probably more appropriate to consider these compounds as similar to their $PbSb_2O_6$ counterparts with extra A-site cations stuffed between the M_2O_6 layers. The electronic structure and physical properties of the stuffed-$PbSb_2O_6$ phases should be more two-dimensional in character. In both cases, the face sharing topology produces a distorted octahedral environment about the M-site cation, although this effect appears to be larger among compounds in the ordered corundum category. The compound $AgBiO_3$ does not fit cleanly into either grouping. The large ionic radii mismatch produces a crystal structure that closely resembles the structure of $NaBiO_3$, but the relatively similar electronegativities of Ag and Bi should give rise to an electronic structure that is three-dimensional. Finally, we note that just as the trirutile structure gives way to the $PbSb_2O_6$ structure as the size of the A-site cation increases, among the $ASnO_3$ compositions, the ilmenite structure gives way to the perovskite structure as the size of the A-site cation increases. Both $CaSnO_3$ and $CdSnO_3$ are polymorphic. The electronic properties of the perovskite forms of these two compounds have been previously considered.[9] Interestingly, the perovskite structure is generally not observed for $ASbO_3$ and $ABiO_3$ compounds, even when ionic radii considerations would normally favor perovskite. The reasons for this behavior are rooted in covalent bonding interactions and have been considered elsewhere.[36,37,38]

3.2 Optical Absorption. The samples prepared in this study have a variety of colors, as shown in Table 7. To more accurately quantify the optical band gaps of these compounds, diffuse reflectance spectra were collected on powder samples. The room-temperature optical absorption spectra of rutile/trirutile, $PbSb_2O_6$-type, and ilmenite powders are shown in Figure 2. Numerical band gap (E_g) values were determined from these data and are listed in Table 7. For those compounds where band gaps have been reported in the literature, SnO_2,[39] β-PbO_2,[40] $MgBi_2O_6$,[41] $ZnBi_2O_6$,[41] and $CdSb_2O_6$,[13] our values are in reasonably good agreement with the previously reported values.

Among the AM_2O_6 trirutile compositions, the band gap increases upon replacing Bi^{5+} with Sb^{5+}, and to a lesser extent upon replacing Zn^{2+} with Mg^{2+}. The former effect can be attributed primarily to differences in the way that main group elements in the fifth and sixth periods bond with oxygen and can be attributed primarily to relativistic effects.[42] A similar trend is observed in the band gaps of SnO_2 (E_g = 3.8 eV) and β-PbO_2 (E_g = 1.7 eV). The change that is observed upon substituting Zn^{2+} for Mg^{2+} originates from the $3d^{10}4s^0$ electron configuration of Zn^{2+} and will be explored in greater detail using band structure calculations. β-PbO_2, $MgBi_2O_6$, $ZnBi_2O_6$, and $ZnSb_2O_6$ show additional absorption in near-IR region. This is a characteristic feature of transparent conductors. It is ascribed to the excitations originating from the plasma frequency due to free electrons in the conduction band. The free carriers are thought to arise from the presence of a small oxygen deficiency. This near-IR absorption is partially responsible for the greenish color observed in $ZnSb_2O_6$.

Similar trends are seen for the $PbSb_2O_6$-type oxides. The ABi_2O_6 phases have band gaps that are ~3 eV smaller than the band gaps of the corresponding ASb_2O_6 analogues. The band gaps of the alkaline-earth antimonates are quite large, whereas the band gap of $CdSb_2O_6$ is markedly smaller. As the $Sb_2O_6^{2-}$ framework is not dramatically different in $CdSb_2O_6$, this effect must originate from Cd^{2+} playing an active role in the electronic structure. This effect is similar to the one seen with Zn^{2+} in the trirutile compositions. The origin of the preedge feature observed for $CaSb_2O_6$, $SrSb_2O_6$, $BaSb_2O_6$, and $CdSb_2O_6$ is not known, but it is likely to be associated with some type of crystal defect.

(36) Blasse, G. *J. Inorg. Nucl. Chem.* **1964**, *26*, 1191.
(37) Goodenough, J. B.; Kafalas, J. A. *J. Solid State Chem.* **1973**, *6*, 493.
(38) Mizoguchi, H.; Woodward, P. M.; Byeon, S.-H.; Parise, J. B. *J. Am. Chem. Soc.* **2004**, *126*, 3175.
(39) Nagasawa, M.; Shionoya, S. *J. Phys. Soc. Jpn.* **1971**, *30*, 158.
(40) Mindt, W. *J. Electrochem. Soc.* **1969**, *116*, 1076.
(41) Mizoguchi, H.; Bhuvanesh, N. S. P.; Woodward, P. M. *Chem. Commun.* **2003**, 1084.
(42) Pyykkö, P. *Chem. Rev.* **1988**, *88*, 563.

Table 6. Structural Features of Ilmenites and In_2O_3 (Corundum Form)

compound	$M-O^a$ distances (Å)	$A-O^a$ distances (Å)	$M-O-M$ angles (deg)	$M-O-A$ angles (deg)	$A-O-A$ angles (deg)	$M-M$ distance (Å)	$A-M$ distance
$CaSnO_3$[20]	3 × 2.01 3 × 2.06	3 × 2.29 3 × 2.56	102.7	88.0	86.3	3.187	3.236
$ZnSnO_3$[19]	3 × 2.010 3 × 2.159	3 × 2.072 3 × 2.199	96.2	83.4	92.8	3.104	2.899
$CdSnO_3$	3 × 2.06(1) 3 × 2.19(1)	3 × 2.18(1) 3 × 2.41(1)	96.5(4)	86.8(4)	91.5(3)	3.170(6)	3.169(2)
$NaSbO_3$[14]	3 × 1.981 3 × 2.005	3 × 2.313 3 × 2.534	100.3	88.1	81.7	3.06	3.178
$KSbO_3$[15]	3 × 1.957 3 × 2.095	3 × 2.464 3 × 2.968	99.9	89.9	71.6	3.102	3.551
$NaBiO_3$[10]	3 × 2.094 3 × 2.137	3 × 2.396 3 × 2.471	99.5	86.6	85.1	3.265	3.169
$AgBiO_3$[10]	3 × 2.109 3 × 2.128	3 × 2.355 3 × 2.685	100.8	88.2	86.2	3.265	3.372
In_2O_3[21]	3 × 2.116 3 × 2.158		95.7	87.2		3.243	3.114

[a] In ilmenite, the oxygen is coordinated by two *M* cations and two *A* cations, and the distances are the ones shown in the second and third columns. For example, in $CaSnO_3$, the O is coordinated by two Sn atoms at distances of 2.013 and 2.065 Å and two Ca atoms at distances of 2.292 and 2.567 Å.

Table 7. Optical Band Gaps of Binary and Ternary Oxides Containing Sn^{4+}, Sb^{5+}, and Bi^{5+}

compound	structure type	color	observed E_g (eV)	calculated E_g (eV)[d]
SnO_2	rutile	white	3.8[a]	2.3
β-PbO_2	rutile	dark brown	1.7[b]	
$MgSb_2O_6$	trirutile	white	4.3	2.4
$ZnSb_2O_6$	trirutile	yellowish green	3.5	1.8
$MgBi_2O_6$	trirutile	reddish brown	1.8	0.8
$ZnBi_2O_6$	trirutile	brown	1.7	
$CaSb_2O_6$	$PbSb_2O_6$	white	5.0	3.8
$SrSb_2O_6$	$PbSb_2O_6$	white	5.0	4.0
$BaSb_2O_6$	$PbSb_2O_6$	white	(>5.5)	
$CdSb_2O_6$	$PbSb_2O_6$	yellowish green	3.8[c]	2.1
$SrBi_2O_6$	$PbSb_2O_6$	brown	2.0	
$BaBi_2O_6$	$PbSb_2O_6$	orange	2.6	
$CaSnO_3$	ilmenite	white	4.4	4.0
$ZnSnO_3$	ilmenite	white	3.7	2.1
$CdSnO_3$	ilmenite	dull yellow	3.1	1.8
$NaSbO_3$	ilmenite	white	4.9	3.7
$KSbO_3$	ilmenite	white	4.8	
$NaBiO_3$	ilmenite	orange	2.7	1.9
$AgBiO_3$	ilmenite	black	0.8	0 (−0.5)
In_2O_3 ($R\bar{3}c$)	corundum	dull white	3.1	1.5

[a] The E_g reported in the literature for single-crystal SnO_2 is 3.8 eV (see ref 39). [b] The E_g reported in the literature for thin film β-PbO_2 is 1.7 eV (see ref 40). [c] The E_g for $CdSb_2O_6$ in thin film form is reported as either 3.8 or 4.4 eV (see ref 13 for further details). [d] Calculated using the LMTO program.

The ilmenite group offers a direct comparison of the three cations that are the focus of this study: Sn^{4+}, Sb^{5+}, and Bi^{5+}. The comparison is most relevant among those compounds containing electropositive *A*-site cations (compounds that fall into the stuffed-$PbSb_2O_6$ category): $KSbO_3$, $NaSbO_3$, $CaSnO_3$, and $NaBiO_3$. Here, we see that the band gaps of the $ASnO_3$ and $ASbO_3$ phases are large and similar to each other, while the band gap of $NaBiO_3$ is ~2 eV smaller. The active role of the *A*-site cation can be seen in those compounds where the *A*-site cation has a $(n-1)d^{10}ns^0$ electron configuration: $ZnSnO_3$, $CdSnO_3$, and $AgBiO_3$. A qualitative comparison suggests that Cd^{2+} and Ag^+ give rise to a larger *A*-site inductive effect than Zn^{2+}. It is worthwhile to note that the band gap of $CdSnO_3$ is nearly the same as that of In_2O_3. Band structure calculations are used to investigate this effect in more detail in the following sections.

3.3 Molecular Orbital Calculations. The band gap of a semiconductor/insulator depends on the position and width of the valence and conduction bands. These are the extended solid equivalents of the HOMO and LUMO in molecular compounds. To understand the relationship between chemical bonding, crystal structure, and optical band gap, we performed electronic band structure calculations. Before presenting the details of the band structure calculations, it is instructive to consider molecular orbital calculations on the structural building blocks, isolated MO_6 octahedra. Figure 3a shows the molecular orbital diagram of an isolated SnO_6^{8-} octahedron.[43] The O 2s orbitals have been omitted because their energy level is considerably lower than the Sn 5s and 5p orbitals limiting the degree of mixing. Nonetheless, the O 2s orbitals are not completely inert, a point we will return to later. The 5s and 5p orbitals of Sn form covalent interactions with the O 2p orbitals, giving rise to bonding and antibonding states. The Sn 5s orbital has a more favorable energetic overlap with the O 2p orbitals than do the Sn 5p orbitals. The antibonding orbital that results from the Sn 5s to O 2p interaction is the LUMO, while nonbonding O 2p states make up the HOMO. The Sn 5s orbital makes the major contribution to the LUMO, but the oxygen character is nonnegligible. The O 2p character of the LUMO will increase as the electronegativity of the metal ion increases. Nonetheless, in a very loose sense the lowest energy electronic transition can be described as oxygen-to-metal charge transfer. More accurately, it is a transition from an O 2p nonbonding orbital to an Sn 5s to O 2p σ^* molecular orbital. The corresponding MO diagrams for SbO_6^{7-} and BiO_6^{7-} octahedra are shown in Figure 3b,c, respectively. Sb^{5+} is more electronegative than Sn^{4+}, and the Sb−O distance is shorter than the Sn−O distance. Consequently, the energetic and spatial overlap of the Sb 5s orbitals with the O 2p orbitals is improved, with respect to the Sn 5s to O 2p interaction. The increased overlap leads to a more covalent cation−anion interaction, accompanied by an increase in the oxygen character of the Sb 5s to O 2p σ^* MO. The energy level of the LUMO

(43) Cotton, F. A. *Chemical Applications of Group Theory,* 3rd ed.; John Wiley & Sons: New York, 1990.

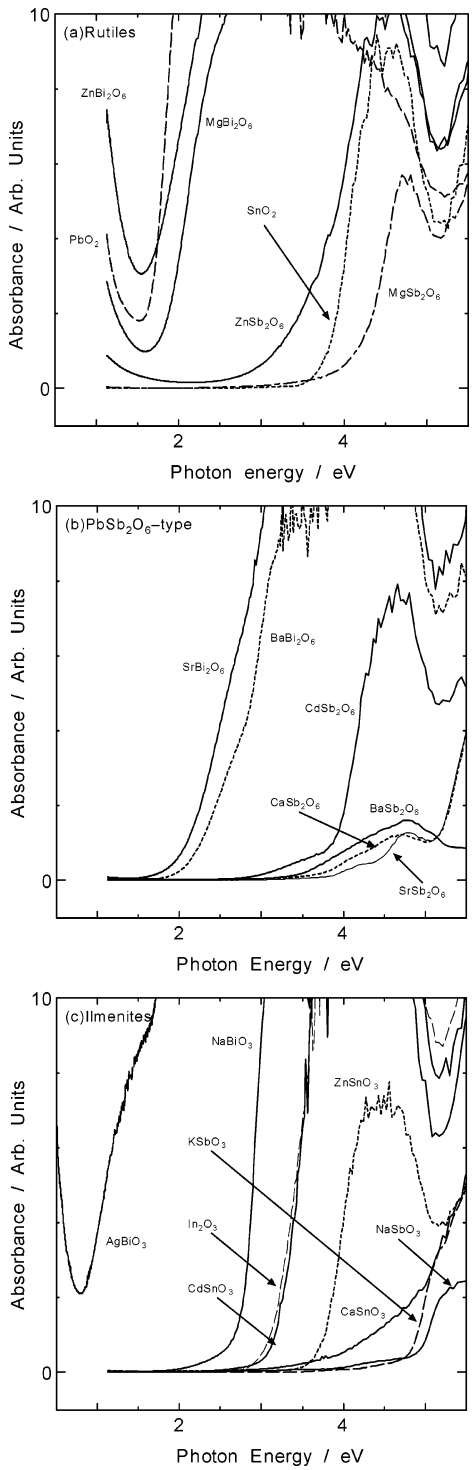

Figure 2. Diffuse reflectance spectra for ternary stannate, antimonite, and bismuthate compounds belonging to (a) the rutile family, (b) the $PbSb_2O_6$-type family, and (c) the ilmenite family.

is lowered by the increased electronegativity of the Sb 5s orbital but is raised by the increased antibonding character of this MO. Apparently, the two effects tend to offset each other so that the HOMO−LUMO splitting is roughly the same for Sn^{4+} and Sb^{5+} octahedra. The energy levels of the Bi^{5+} cation are somewhat different. Relativistic effects lower the energy level and decrease the spatial extent of the Bi 6s orbitals, with respect to the 5s orbtials of Sn and Sb. Both changes reduce the Bi 6s to O 2p overlap, decreasing the antibonding character of the LUMO and thereby substantially lowering its energy level. These effects lead to an increase in the O 2p character present in the LUMO.

3.4 Band Structure Calculations. While the molecular orbital picture is a useful starting point, band structure calculations are necessary to fully understand the electronic structure. We utilized the LMTO code developed by Andersen and co-workers to carry out band structure calculations for this purpose.[25] To assist in understanding the nomenclature of reciprocal space, Brillouin zones for primitive tetragonal (rutile, trirutile) and trigonal/hexagonal ($PbSb_2O_6$-type) lattices are shown in Figure 4. The special points noted in these diagrams will be useful as the discussion proceeds. First of all, consider the agreement between calculated and observed band gaps. The calculated band gaps are systematically related to the experimentally observed values, as shown in Figure 5. Unfortunately, the calculated band gaps are consistently too small by approximately 0.5−2.0 eV, a level of discrepancy not unusual for oxides.[9,44] On the basis of earlier studies,[9,44] it appears that the underestimation of the band gap stems from an overestimation of bandwidth, but this hypothesis has not been investigated in detail. Despite the failure of the calculations to predict band gaps in an absolute sense, they do reproduce a number of the trends noted in the optical data. First of all, the band gap increases in the order, bismuthate $\ll$ stanate $\leq$ antimonate. Second, the trirutile compounds have smaller band gaps than the corresponding $PbSb_2O_6$ and ilmenite compositions. Finally, the presence of Zn^{2+}, Cd^{2+}, and Ag^{+} on the *A*-site leads to a significant decrease in the band gap. However, what makes the calculations most useful is the ability to pinpoint the bonding interactions that control the electronic structure. To do so, we need to delve deeper into the results of the LMTO calculations.

3.4.1. Rutile Structure. As stated in the Introduction, SnO_2 is one of the most widely utilized TCO materials. The electronic band structure and density of states for SnO_2 are shown in Figure 6. In Figure 6a,b, fatbands are used to highlight the orbital contributions to each band. The width of the hatching corresponds to the contribution of a particular atomic orbital to the band in question. Fatbands are a useful tool to quantify the change in orbital contribution from band to band and within a given band upon moving through reciprocal space. The partial density of states (PDOS) plot shown in Figure 6c is simply a summation of the orbital character of all bands at a given energy. In this figure, and throughout the rest of the paper, the binding energy ($E = 0$) is referenced to the valence band (VB) maximum. The horizontal axis scale is inversely proportional to the length of the unit cell in various directions.

Most features of the calculated band structure agree well with previous reports.[45] For SnO_2, the VB maximum is located at the *R* point, while the conduction band (CB) minimum is located at the Γ point, indicating that SnO_2 should be a semiconductor with an indirect band gap of 2.3 eV. The fatband plots show that the valence band (VB) is primarily O 2p in character. The

(44) Eng, H. W.; Barnes, P. W.; Auer, B.; Woodward, P. M. *J. Solid State Chem.* **2003**, *175*, 94.

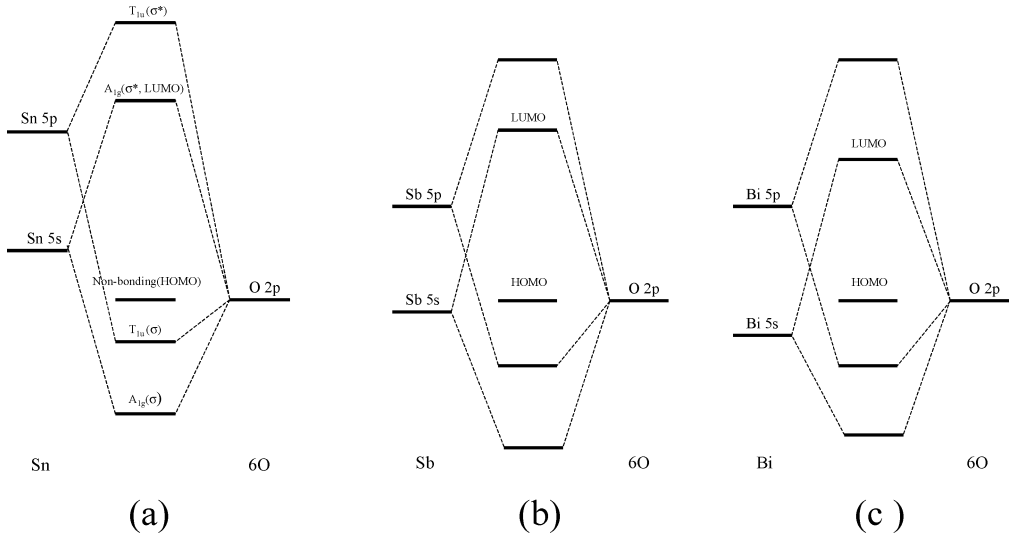

Figure 3. Molecular orbital diagram for an isolated MO_6^{n-} octahedron, where M is (a) Sn^{4+}, (b) Sb^{5+}, or (c) Bi^{5+}. For clarity, interactions involving the O 2s orbitals have been omitted.

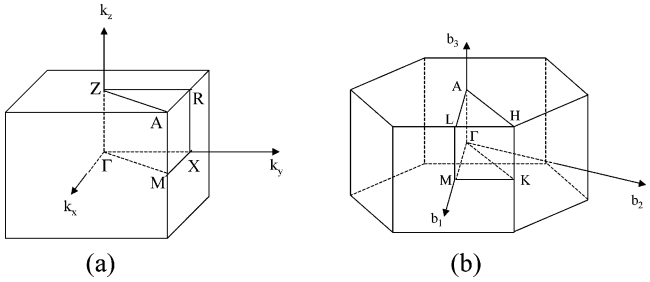

Figure 4. Brillouin zones for (a) a primitive tetragonal lattice and (b) a hexagonal lattice.

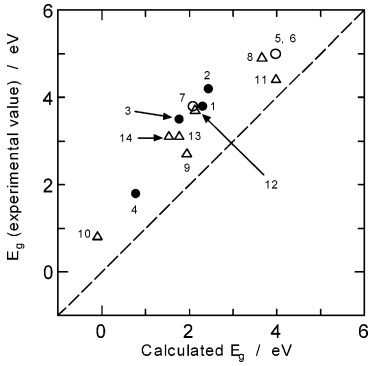

Figure 5. Relation of the estimated band gap from diffuse reflectance and that calculated by LMTO code. Numbers identify the compound in question as follows. 1: SnO_2, 2: $MgSb_2O_6$, 3: $ZnSb_2O_6$, 4: $MgBi_2O_6$, 5: $CaSb_2O_6$, 6: $SrSb_2O_6$, 7: $CdSb_2O_6$, 8:$NaSbO_3$, 9: $NaBiO_3$, 10: $AgBiO_3$, 11: $CaSnO_3$, 12: $ZnSnO_3$, 13: $CdSnO_3$, and 14: In_2O_3 (corundum form). The dashed line represents perfect agreement between calculations and experiment.

nonbonding character of these bands is particularly pronounced over the region of 0.0 to −2.0 eV. The small amount of dispersion that is present comes from weak antibonding O 2p to O 2p interactions in the closed packed oxygen lattice. On the other hand, the CB is predominantly Sn 5s in character with a significant admixing of O 2p states. Near the CB minimum, the O 2p contribution is minimal, but a small contribution from the O 2s orbitals can be seen. This description is in qualitative agreement with the predictions of the molecular orbital diagram shown in Figure 3a, with one exception. The negligible O 2p contribution at the CB minimum is not expected from the MO diagram. This feature originates in the translational symmetry of the rutile structure and will be discussed in detail next.

The CB shows a large dispersion, particularly near the CB minimum at the Γ point. This implies that carriers in doped SnO_2 should have a high mobility because the effective mass of a carrier, m^*, is inversely proportional to the second derivative of the E versus k curve (wide bands give rise to highly mobile carriers). It is well-known that high carrier mobility is a critically important property for application as a transparent conductor. Another interesting feature of the band structure is the fact that near the Γ point the CB minimum is separated from the next highest level in the CB by nearly 5 eV. Freeman et al. have suggested that this is an important feature of a good transparent conductor because it limits the optical absorbance across the visible and IR regions of the spectrum.[46] The bands higher than +8 eV have Sn 5p character mainly and are clearly split from the two Sn 5s to O 2p σ^* bands. The lowest energy conduction band has a large dispersion along both the Γ to Z and Γ to M directions. In real space, the Γ to Z line corresponds to a direction parallel to the c-axis, while the Γ to M line runs perpendicular to the c-axis. In our calculations, the dispersion along Γ to Z is only slightly larger than Γ to M. This result is an indicator of the three-dimensional character of the electronic structure. It is also consistent with experimental measurements of the effective carrier masses of 0.234 m_e parallel to the c-axis and 0.299 m_e perpendicular to the c-axis.[47] If direct Sn 5s to Sn 5s bonding within the edge-sharing rutile chain plays an important role near the CB minimum, one would expect the effective mass to be much smaller for carrier transport parallel to the chain direction (along the c-axis). How-

(45) (a) Arlinghaus, F. J. *J. Phys. Chem. Solids* **1974**, *35*, 931. (b) Robertson, J. *J. Phys. C* **1979**, *12*, 4767. (c) Mishra, K. C.; Johnson, K. H.; Schmidt, P. C. *Phys. Rev. B* **1995**, *51*, 13972.

(46) Mryasov, O. N.; Freeman, A. J. *Phys. Rev. B* **2001**, *64*, 233111.

(47) Button, K. J.; Fonstad, D. G.; Dreybradt, W. *Phys. Rev. B* **1971**, *4*, 4539.

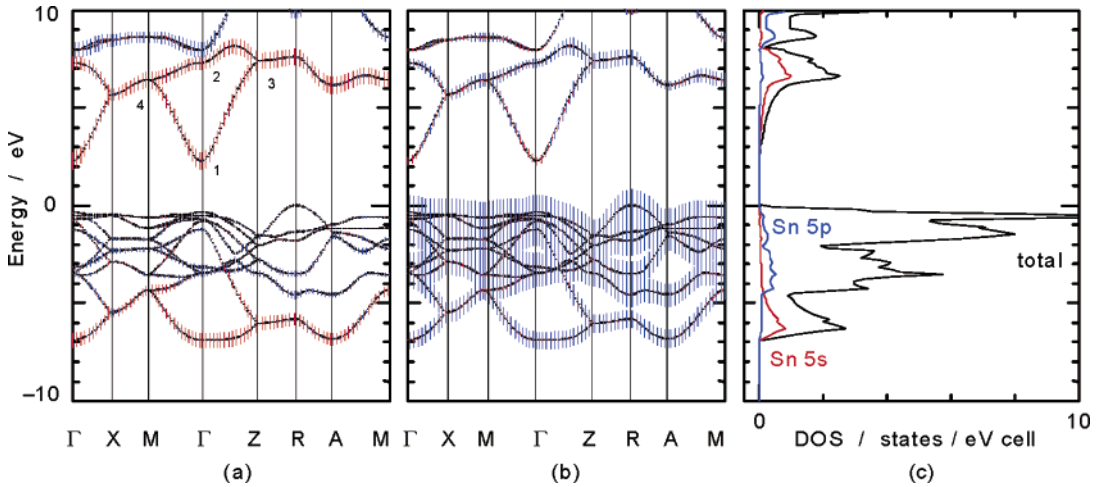

Figure 6. Calculated band structure of SnO_2. (a) The fatbands on the left-hand side show the Sn 5s orbital contribution in red and the Sn 5p orbital contribution in blue. (b) The fatbands in the middle show the O 2s orbital contribution in red and the O 2p orbital contribution in blue. The orbital overlap at the points labeled 1−4 is shown in Figure 8. (c) The partial density of states (PDOS) plot is shown on the right-hand side, with the Sn 5s contribution in red, the Sn 5p contribution in blue, and the total electronic DOS in black.

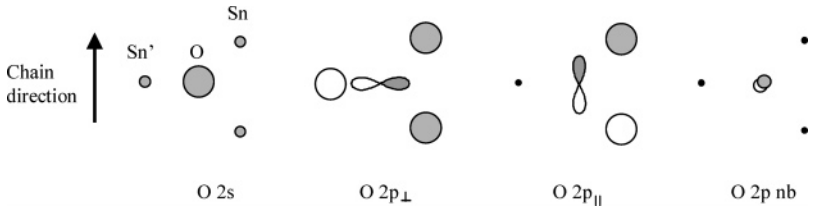

Figure 7. Overlap of the oxygen 2s and 2p orbitals with the surrounding Sn 5s orbitals.

ever, the band structure calculations and experimental measurements suggest that Sn−Sn interactions are not responsible for the disperse CB.

To understand how the electronic structure of an isolated octahedron (Figure 3a) evolves into the band structure of an extended solid (Figure 6), it is necessary to consider how the octahedra are connected. The polyhedral connectivity is intimately linked to the anion coordination, so let us begin with an examination of the bonding at oxygen. The unit cell of SnO_2 is made of two $(SnO_2)^0$ chains, so-called rutile chains, which are related by a 2-fold screw rotation axis. In the rutile structure, each oxygen ion is coordinated by two tin atoms within a chain (intrachain bonding) and one tin atom from a neighboring chain (interchain bonding). The coordination environment can be described as a Y-shaped planar $Sn'OSn_2$ unit, where the Sn′ symbolizes a tin atom on the neighboring chain. The oxygen site symmetry is C_{2v}. The bonding overlap between the 2s and 2p orbitals on the central oxygen with the Sn 5s orbitals is illustrated in Figure 7. The O 2s orbital can form bonding and antibonding interactions with tin as long as the Sn 5s orbitals on neighboring chains (Sn and Sn′) are in phase with each other, whereas the orbital labeled O 2p ⊥ needs the Sn 5s orbitals on neighboring chains to be out of phase with each other to form effective bonding and antibonding interactions. The symmetry of the orbital labeled O 2p || allows bonding interactions with Sn but not with Sn′. Consequently, this orbital will contribute to the intrachain bonding but not to the interchain bonding. Finally, the symmetry of the orbital labeled O 2p *nb* is such that it cannot mix with the Sn 5s orbitals.

The notation used in the previous paragraph can be used to describe the orbital overlap at four key points in the conduction band of SnO_2. These points are labeled in Figure 6a, and the orbital overlap at each point is shown in Figure 8. Points 1 and 2 both fall at the Γ point and correspond to the two lowest energy conduction bands, with respective energies of +2.3 and +7.4 eV. At the Γ point, translational symmetry dictates that the phase of all Sn 5s orbitals in a given chain must be the same. In that case, the intrachain Sn 5s to O 2p || orbital interaction is not allowed by symmetry, and as explained previous, the O 2p || orbitals make no contribution to the interchain bonding. As a result, the O 2p || orbitals make no contribution at points 1 and 2. Next, consider the interaction between the Sn 5s and O 2p ⊥ orbitals. When the phases of the Sn 5s orbitals on neighboring chains are opposite, the O 2p ⊥ orbital can form strong σ^* interactions with all three of the surrounding Sn atoms, as shown in Figure 7. This overlap corresponds to point 2 in the SnO_2 band structure and is shown in Figure 8c. The strong antibonding interaction is responsible for the relatively high energy level of this point (+7.4 eV). On the other hand, when the tin atoms on neighboring chains have the same phase, the O 2p ⊥ orbital makes a σ^* intrachain interaction and a σ interchain interaction. The two interactions tend to cancel out, and the net interaction is close to a nonbonding one. As a result, the contribution of the O 2p ⊥ orbital at point 1 is minimal as shown in Figure 8b. Thus, we see that interchain interactions are responsible for essentially eliminating the Sn 5s to O 2p antibonding interactions at the CB minimum. However, the fatband representation shown in Figure 6

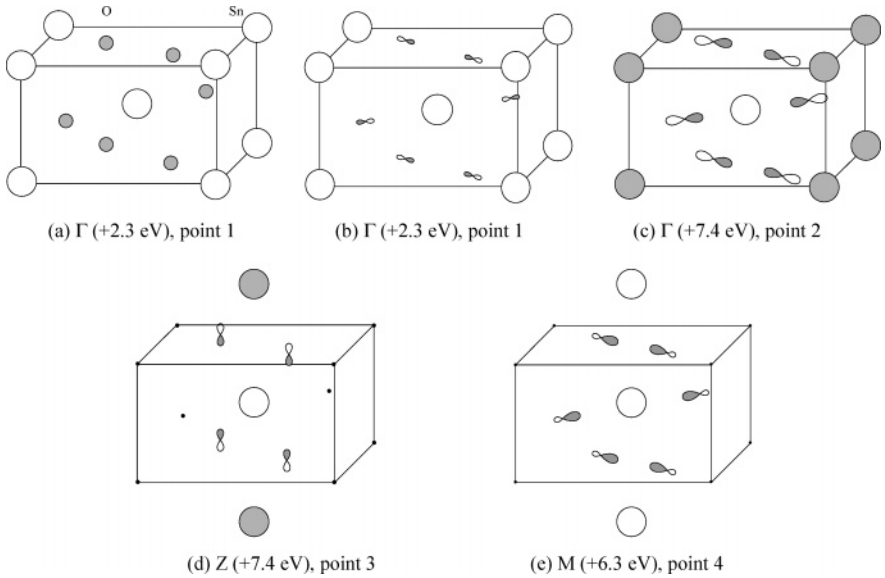

Figure 8. Orbital interactions for special points in the conduction band of SnO_2: (a) Sn 5s to O 2s overlap, (b) Sn 5s to O 2p overlap at the CB minimum (point 1), (c) the Sn 5s to O 2p overlap at Γ for the 2nd lowest energy CB (point 2), the Sn 5s to O 2p overlap at (d) Z (point 3), and (e) M (point 4). Each point corresponds to the locations in the band structure labeled in Figure 6a.

indicates that the O 2s orbitals play a nonnegligible role at the CB minimum. The Sn 5s to O 2s σ^* interaction at point 1 is shown in Figure 8a. There is no frustration, and the interaction is fully antibonding. However, the strength of this interaction is diminished by the relatively poor energetic overlap of the Sn 5s and O 2s orbitals. Nonetheless, the calculations clearly indicate that the Sn 5s to O 2s σ^* interaction raises the energy level of the CB minimum, thereby increasing the band gap and decreasing the CB dispersion.

The two lowest unoccupied bands become degenerate at the *Z* (point 3) and *M* (point 4) points, giving rise to the large dispersion of the lowest energy band. At the *Z* point, the two bands of Sn 5s origin are degenerate ($E = +7.4$ eV). The real part of the orbital interaction for one of the two bands is shown in Figure 8d. We can see strong intrachain antibonding along the rutile chain direction due to Sn 5s to O 2p || σ^* interactions. This raises the energy of the CB and is responsible for the large dispersion of the lowest energy CB along the Γ to *Z* line. The degenerate band has a very similar orbital overlap. Note that the O 2p ⊥ contribution, along with the interchain interaction, nearly vanishes at the *Z* point. The real part of the orbital interaction at the *M* point for one of two degenerate bands is shown in Figure 8e. There is strong antibonding along the rutile chain direction due to Sn 5s to O 2p ⊥ σ^* and Sn 5s to O 2s σ^* intrachain interactions. The lack of strong interchain antibonding interactions explains why the degenerate bands at *M* (point 4, $E = +6.3$ eV) are not destabilized as much as the higher band at Γ (point 2, $E = +7.4$ eV).

Up to this point, the Sn 5s to Sn 5s interactions have been neglected. Do they play a significant role? A measure of the importance of the Sn 5s to Sn 5s interaction can be extracted from the dispersion or lack thereof of the second lowest energy band in the CB. The orbital overlap of the second lowest energy band is shown at the Γ point in Figure 8c and at the *Z* point in Figure 8d. While there are strong Sn 5s to O 2p antibonding interactions at both points, as already discussed, the Sn 5s to Sn 5s interaction is bonding at Γ and antibonding at *Z*. If the Sn 5s to Sn 5s interaction played an important role, the energy level of this band at *Z* should be considerably higher than it is at Γ. Inspection of Figure 6 shows that in fact these two points have very similar energies. Thus, we conclude that while the Sn 5s to Sn 5s interaction may play a role in the transport properties of doped samples, it is not responsible for the presence of a disperse CB in SnO_2. Rather, it seems that the oxygen coordination is primarily responsible for the wide CB that makes SnO_2 such an effective TCO material.

3.4.2. Trirutile Structure—$MgSb_2O_6$, $ZnSb_2O_6$, and $MgBi_2O_6$. Although the rutile and trirutile structures are closely related, at first glance their electronic structures appear quite different. To better compare electronic structures of the two structure types, it is useful to show how the special points in reciprocal space of the rutile structure map onto the trirutile structure. This is done in Figure 9. The simple rutile structure has two formula units per unit cell and tetragonal lattice parameters of $a \times a \times c$. The trirutile structure has six formula units per unit cell and tetragonal lattice parameters of $a \times a \times 3c$ (see Figure 1b). Thus, the volume of the first Brillouin zone of trirutile is one-third that of rutile. In Figure 9a, the band folding of the CB along the Γ−*Z* direction for an Sn_3O_6 ($Z = 2$) artificial supercell is illustrated. The two bands for SnO_2 are folded twice to produce six bands. Next, Sn_3O_6 is converted to AM_2O_6 (i.e., $MgSb_2O_6$) by cationic ordering. In this process, the two bands that originate from *A* *n*s orbitals move higher in energy because of the electropositive character of *A*-site cation, as shown in Figure 9b. Finally, the oxygen position is modified slightly in response to the cationic ordering to complete the trirutile band structure. The lower part of the CB for $MgSb_2O_6$ has four bands instead of two as a result of the fact that there are now four Sb^{5+} ions in the unit cell, while the two highest energy bands are derived primarily from the more electropositive Mg^{2+} cation.

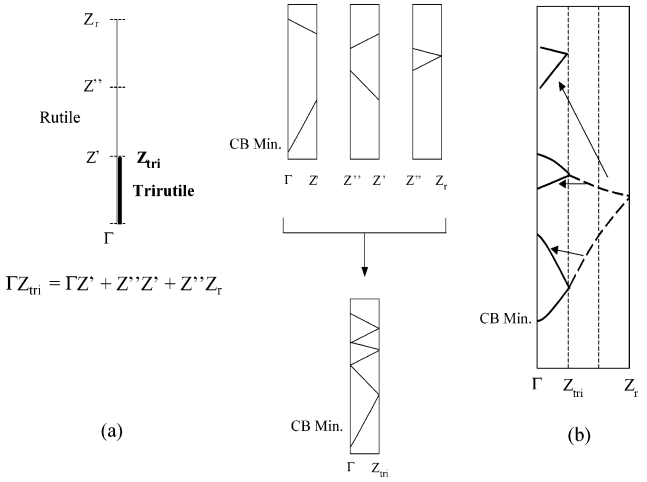

Figure 9. (a) Conversion of Brillouin zone from rutile SnO_2 ($Z = 2$) to trirutile Sn_3O_6 ($Z = 2$). The Sn 5s bands near the bottom of the CB for Sn_3O_6 are shown on the right. The band folding associated with tripling the *c*-axis can clearly be seen. (b) Schematic electronegativity effect in the E vs k diagram along Γ to Z line for the s bands near the bottom of the CB upon changing from Sn_3O_6 to AM_2O_6.

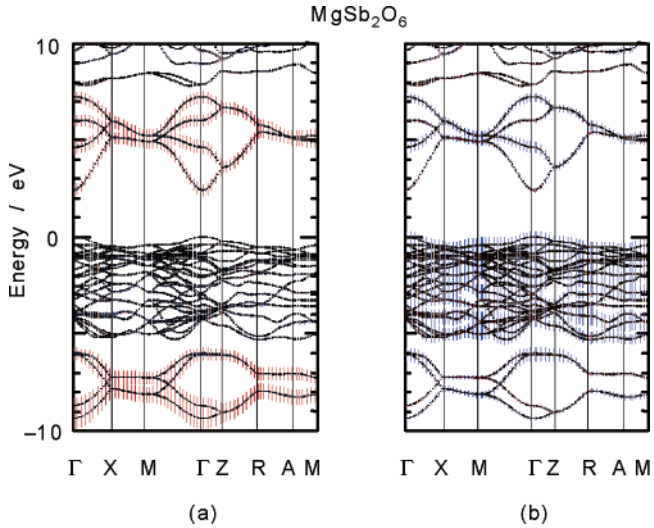

Figure 10. Calculated band structure of $MgSb_2O_6$. The fatbands on the left-hand side show the Sb 5s (red) orbital contribution and the Mg 3s (blue) orbital contribution to the band structure. The fatbands on the right-hand side show the O 2s (red) orbital contribution and the O 2p (blue) orbital contribution for oxygen (4f site) to the band structure.

The additional bands that result upon increasing the size of unit cell can be explained through the concept of band folding.

Figure 10a,b shows the E versus k diagram and fatband representation for the trirutile compound $MgSb_2O_6$, as obtained from LMTO calculations. The diffraction analysis suggested that $MgSb_2O_6$ has a small amount of cation disorder present, (see Table 1), but this perturbation was neglected in the calculations. As before, the top of the VB has been set to 0 eV. Although the E versus k diagram for $MgSb_2O_6$ looks complicated at first glance, the complexity originates from the aforementioned band folding. Once the band folding is taken into account, the electronic structure of $MgSb_2O_6$ is seen to be similar to SnO_2, with some notable differences. The calculations suggest that $MgSb_2O_6$ will be a direct-gap semiconductor with a band gap of 2.4 eV. This value is similar to the calculated indirect band gap of 2.3 eV calculated for SnO_2. Figure 10a shows the fatband contributions of the Sb 5s and Mg 3s orbitals, while Figure 10b shows the contributions of the O 2s and O 2p orbitals. The Sb 5s-fatband splits into two regions: the Sb 5s to O 2p σ bonding states are located over the energy range −9.3 to −6.0 eV, which is deeper than the Sn 5s to O 2p σ bonding states in SnO_2. The stabilization of the Sb 5s to O 2p σ bonding bands follows from the increase in cation electronegativity upon going from Sn^{4+} to Sb^{5+}. The corresponding antibonding bands are located in the region of +2.4 to +7.2 eV. The width of the conduction band is somewhat smaller than that calculated for SnO_2, where the CB spans a range from roughly +2.3 to +8.2 eV. The highly covalent nature of the Sb−O bonds is evident from the observation that the Sb 5s orbitals contribute equally to the bonding and antibonding bands. The bands with energies greater than +7.9 eV can be mainly attributed to the unoccupied Sb 5p states, while the Mg 3s orbital contribution is primarily found at energies higher than +10 eV (not shown).

In the context of designing and/or understanding the features of the electronic band structure that are

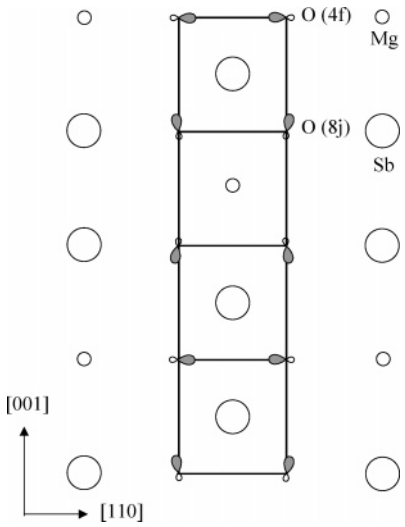

Figure 11. Orbital interactions for $MgSb_2O_6$ at the conduction band minimum, which falls at the Γ point.

favorable for a transparent conductor, it is important to note some important differences between the electronic band structures of $MgSb_2O_6$ and SnO_2. First of all, the lowest energy CB in $MgSb_2O_6$ has a smaller separation from the successive (higher energy) conduction bands. This feature will tend to increase the optical absorbance of a doped sample in the blue and UV regions of the spectrum, potentially limiting the transparency of the material. This behavior can be understood from the band folding arguments described in the proceeding paragraphs. More importantly, in $MgSb_2O_6$, the lowest energy conduction band is not as disperse as is its counterpart in SnO_2, reducing the carrier mobility in the former compound. To better understand this feature, it is instructive to consider the orbital overlap at the CB minimum (at the Γ point). The orbital interaction at the CB minimum is shown in Figure 11. For simplicity, only the (110) plane is shown. Notice that the O 2p orbitals are oriented so as to maximize the antibonding overlap with the Sb 5s orbitals through the

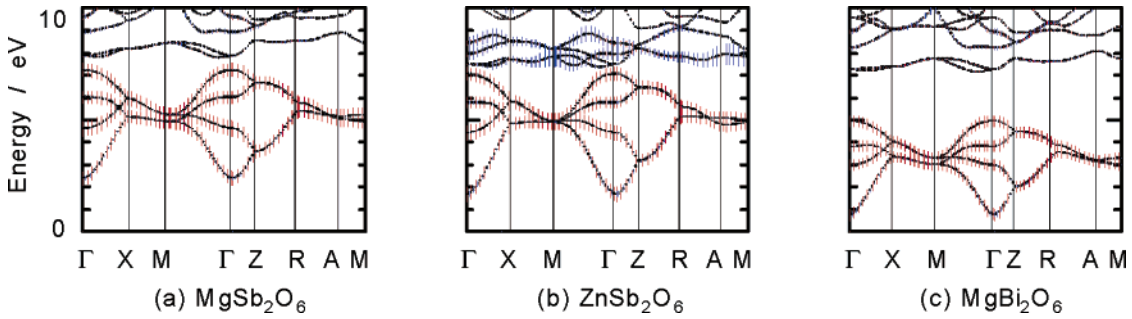

Figure 12. Calculated conduction band structures for (a) $MgSb_2O_6$, (b) $ZnSb_2O_6$, and (c) $MgBi_2O_6$. The fatbands show the Sb 5s/Bi 6s (red) orbital contribution and the Mg 3s/Zn 4s (blue) orbital contribution to the band structure.

shared octahedral edge, while the O 2s orbitals interact in a σ^* sense with both the Sb 5s and Mg 3s orbitals. These features are rather similar to the overlap found at the CB minimum in SnO_2 with one important difference. In SnO_2, the backside lobe of each O 2p $\perp$ orbital overlaps in a bonding fashion with an Sn atom from a neighboring chain. As explained previously, this geometry leads to a near cancellation of the Sn 5s to O 2p σ and σ^* interactions. This is not the case in $MgSb_2O_6$ because the Mg 3s to O 2p σ interaction is much weaker than the Sb 5s to O 2p σ^* interaction, due to the poor energetic overlap of the electropositive magnesium atom with oxygen. As a result, the CB minimum possesses a significantly greater degree of antibonding character with O 2p. This is evident from the fatbands shown in Figure 10b, which show a higher O 2p contribution at the CB minimum than that observed for SnO_2. This contribution destabilizes the CB minimum, increases the band gap, and reduces the CB dispersion. Notice that even when the neighboring SbO_6 octahedra belong to different chains and are connected by a shared corner rather than a shared edge, the orientation of the O 2p orbital at the CB minimum is similar to that seen for the O 2p $\perp$ orbital in SnO_2. It is oriented so that one lobe is directed in a plane containing both antimony ions and oxygen along a line bisecting the Sb−O−Sb bond, as shown in Figure 7. This orientation optimizes both the bonding (in the VB) and antibonding (in the CB) overlap of the O 2p orbital with the two coordinating *M* cations. The antibonding interaction can be largely negated if a third cation is oriented to achieve optimal spatial and energetic overlap with the other lobe of the O 2p orbital. This is the case in SnO_2 but not in $MgSb_2O_6$. For three-coordinate oxygen, this cancellation reaches a maximum for trigonal planar coordination and an *A*-site cation with electronegativity comparable to that of the *M*-site cation.

Because ofthe similar ionic radii of Mg^{2+} (r = 0.72 Å, CN = 6) and Zn^{2+} (r = 0.74 Å, CN = 6),[48] the crystal structures of $MgSb_2O_6$ and $ZnSb_2O_6$ are very similar. Consequently, any differences that arise in the electronic structures can be attributed to changes in the *A*−O interaction and not to distortions of the $Sb_2O_6^{2-}$ network. Although the crystal structures of both compounds are comparable, the band gap of $ZnSb_2O_6$ (3.5 eV) is considerably smaller than that of $MgSb_2O_6$ (4.3 eV) (see Figure 2a). Figure 12b shows the conduction band structure of $ZnSb_2O_6$ (see Supporting Information for the complete band structure). In general, our results are in agreement with the band structure reported by Matsushima et al.[49] The electronic structure of $ZnSb_2O_6$ is qualitatively similar to the electronic structure of $MgSb_2O_6$. Quantitatively, the calculated band gap of $ZnSb_2O_6$ (1.8 eV) is smaller than that of $MgSb_2O_6$ (2.4 eV), consistent with the experimentally observed decrease in band gap. The reduced band gap results from increased CB dispersion, which can in turn largely be traced back to the Zn 4s to O 2p overlap. The Zn^{2+} ion has fully occupied 3d orbitals located at a relatively shallow binding energy, approximately −6 eV, raising the possibility that the Zn 3d to O 2p interaction pushes up the VB maximum. However, the LMTO calculations do not indicate that this interaction plays a significant role in reducing the band gap. Thus, the band gap narrowing can be attributed to the increased width of the CB. The fatbands diagrams in Figure 12 show that the Zn 4s orbitals make a nonnegligible contribution to lowest energy CB near Γ. Thus, we see an inductive effect (active participation of the *A*-site cation in bonding near E_F) in $ZnSb_2O_6$ that lowers the band gap and increases the CB dispersion with respect to $MgSb_2O_6$. The comparative energetic overlap of the Zn 4s and Mg 3s orbitals with the Sb 5s to O 2p σ^* orbital can be seen by comparing Figure 12a,b. The Zn 4s orbital contribution is located primarily between +7.5 and +9.0 eV and can be partially seen in this figure, whereas the Mg 3s orbital contribution occurs largely at energies higher than +10 eV. This explains the larger inductive effect of Zn. In fact, *n*-doped $ZnSb_2O_6$ samples have been shown to possess moderate electrical conductivity and have been studied as a candidate material for high temperature thermoelectric applications.[11]

Next, we examine how the band structure responds to replacing Sb^{5+} with Bi^{5+}. Figure 12c shows the band structure of $MgBi_2O_6$ as obtained from the LMTO calculations. The electronic structure of $MgBi_2O_6$ is qualitatively very similar to $MgSb_2O_6$ and $ZnSb_2O_6$. Quantitatively, though, the calculated band gap of $MgBi_2O_6$ (0.8 eV) is much smaller than that of $MgSb_2O_6$ (2.4 eV). This is consistent with the trend observed in the experimental band gaps, 1.8 eV for $MgBi_2O_6$ and 4.3 eV for $MgSb_2O_6$. The four Bi 6s to O 2p σ bands cover the energy range −6.5 to −9.4 eV (see Supporting Information for the complete band structure), while the four Bi 6s to O 2p σ^* bands span the energy range +0.8 to +5.0 eV. Compared with $MgSb_2O_6$, we see the energy

(48) Shannon, R. D. *Acta Crystallogr., Sect. A.* **1976**, *32*, 751.
(49) Matsushima, S.; Tanizaki, T.; Nakamura, H.; Nonaka, M.; Arai, M. *Chem. Lett.* **2001**, 1010.
(50) Phillips, J. C. *Bonds and bands in semiconductors*; Academic Press: New York, 1973.

ranges covered by both sets of bands are slightly narrower, and the σ/σ^* splitting is reduced somewhat. These features are consistent with a reduction in the Bi 6s to O 2p overlap, with respect to the Sb 5s to O 2p overlap. Interestingly, the Bi 6s orbitals make a larger contribution to the filled Bi 6s to O 2p σ bonding bands, while the O 2p orbitals make a larger contribution to the empty Bi 6s to O 2p σ^* antibonding bands (see Supporting Information). This is consistent with the orbital energy levels depicted in the MO diagram in Figure 3c. The bands found from +7 to +10 eV can be attributed to antibonding Bi 6p to O 2p interactions. These are more widely separated from Bi 6s to O 2p σ^* antibonding bands in $MgBi_2O_6$ than the corresponding bands in $MgSb_2O_6$. The increased M *n*s to M *n*p splitting as well as the decreased σ/σ^* splitting can be attributed to scalar relativistic effects.[42] The relativistic effects lower the energy and reduce the spatial extent of the Bi 6s orbitals, thereby lowering the energy of the CB and decreasing the band gap. The reduced overlap also leads to a small reduction in the CB dispersion. This presents an intrinsic challenge to designing transparent conductors based on Bi^{5+} oxides.[41] It would seem as though the only way to push the band gap out toward the UV portion of the spectrum is to decrease the CB dispersion. Unfortunately, this strategy reduces carrier mobility, which is undesirable. Although calculations were not carried out for $ZnBi_2O_6$, due to the lack of a structural model, it is interesting to note that experimentally $MgBi_2O_6$ and $ZnBi_2O_6$ have similar band gaps (1.8 vs 1.7 eV). This behavior is in contrast to the optical properties of $MgSb_2O_6$ and $ZnSb_2O_6$. Apparently, by lowering the energy of the conduction band via replacement of Sb^{5+} with Bi^{5+}, the energetic overlap of the CB with the empty Zn 4s states is diminished, and the inductive effect is reduced.

3.4.3. $PbSb_2O_6$ Structure—$CaSb_2O_6$ and $CdSb_2O_6$. The topology and symmetry of the $PbSb_2O_6$ structure is quite different from that of rutile, yet the two structures have some similarities. Both structures contain infinite networks of edge-sharing octahedra, chains in the case of rutile and sheets in the case of $PbSb_2O_6$ (see Figure 1). The local oxygen coordination environment in the $PbSb_2O_6$ structure is similar to that seen in trirutile, although the A-cations found in $PbSb_2O_6$ compounds are generally larger and more electropositive. Nevertheless, the band gaps of the ASb_2O_6 compounds examined in this study (A = Ca, Sr, Ba, Cd) tended to be markedly larger than the corresponding ASb_2O_6 trirutile compounds (A = Mg, Zn). In fact, the band gaps of $CaSb_2O_6$ and $SrSb_2O_6$ (E_g ~5 eV) fell at the upper limit of the range that could be reliably accessed with our spectrometer, while the band gap of $BaSb_2O_6$ was too large to measure. The band gap of $CdSb_2O_6$ was noticeably smaller (E_g = 3.8 eV), suggesting that Cd^{2+} plays an active role in the electronic structure, similar to the role Zn^{2+} plays in $ZnSb_2O_6$. The bismuthate compounds, $BaBi_2O_6$ and $SrBi_2O_6$, have much smaller band gaps (E_g ~2 eV), for reasons discussed in the previous section. To investigate the electronic structure of these compounds further and to confirm the inductive effect of Cd^{2+}, band structure calculations are presented below for $CaSb_2O_6$ and $CdSb_2O_6$.

Figure 13a,b shows the electronic band structure, including fatbands, for $CaSb_2O_6$ as obtained from the LMTO band structure calculation. The CB minimum is located at the Γ point, and the calculated band gap is 3.8 eV. The CB is quite narrow, approximately 3 eV wide. The little dispersion that is present is distributed roughly equal along the Γ to A line, which runs parallel to the z-axis of the unit cell (perpendicular to the layers), and the Γ to M line, which runs parallel to [1−10], which corresponds to Sb−Sb direction (within the layers). The fact that some dispersion exists along Γ to A implies that calcium plays some role in the electronic structure of the CB. This is confirmed by the fatbands, which show a small contribution of the Ca 4s orbital at the CB minimum. The fact that the dispersion along Γ to M is not significantly larger than the dispersion along Γ to A indicates that even within the layers, the electron mobility will be very small. The band structure of $SrSb_2O_6$ is similar.

The crystal structure of $CdSb_2O_6$ is quite similar to that of $CaSb_2O_6$, the main difference being the slightly longer A−O bonds found in $CaSb_2O_6$ (see Table 4), a feature that is expected from the slightly larger ionic radius of Ca^{2+}.[48] Yet, the band gap of $CdSb_2O_6$ is ~1.2 eV smaller than $CaSb_2O_6$. As a result, the differences in electronic structure can be directly attributed to the covalent interaction of Cd^{2+} with the $Sb_2O_6^{2-}$ layers. Figure 13c,d shows the band structure, including fatbands, for $CdSb_2O_6$. The calculated electronic structure of $CdSb_2O_6$ is qualitatively similar to that of $CaSb_2O_6$. However, the CB is considerably more disperse (~4 vs ~3 eV), and the band gap is smaller (2.1 vs 3.8 eV). The Cd^{2+} ion has fully occupied 4d orbitals located at a relatively shallow binding energy, near −5.5 eV in Figure 13. The LMTO calculation suggests that the Cd 4d to O 2p interaction pushes up the energy of the VB maximum by roughly 0.5−1.0 eV. The remaining 0.7−1.2 eV decrease in the band gap can be attributed to the increased width of the CB. The fatbands in Figure 13c show that the Cd 5s and Sb 5s orbitals both make major contributions to the lowest energy CB. Furthermore, the O 2p contribution at the CB minimum is minimal and markedly reduced with respect to $CaSb_2O_6$ (Figure 13b). These are the same features seen in the electronic structures of $ZnSb_2O_6$ and SnO_2. The orbital interactions that lower the energy of the CB minimum at Γ are similar in all three compounds. In the case of $CdSb_2O_6$ at the CB minimum, there is a bonding overlap of the empty Cd 5s orbital with the backside lobe of the O 2p ⊥ orbital involved in an antibonding interaction with two Sb 5s orbitals across a shared octahedral edge. The orbital interactions along the Γ to A line are summarized schematically in Figure 14. Just as in SnO_2, as one moves away from Γ, the bonding Cd 5s overlap with the antibonding Sb 5s to O 2p ⊥ states decreases, and the lowest energy CB is destabilized, creating dispersion in this band. Further evidence for the increased dispersion of the CB in $CdSb_2O_6$ comes from the report that n-doped $CdSb_2O_6$ samples (doping occurs through Y substitution onto the Cd site) possess high electronic conductivity.[13]

3.4.4. Ilmenite Structure—$NaBiO_3$, $AgBiO_3$, $CdSnO_3$, and In_2O_3. As discussed in section 3.1, the ilmenite compounds can be divided into two groups.

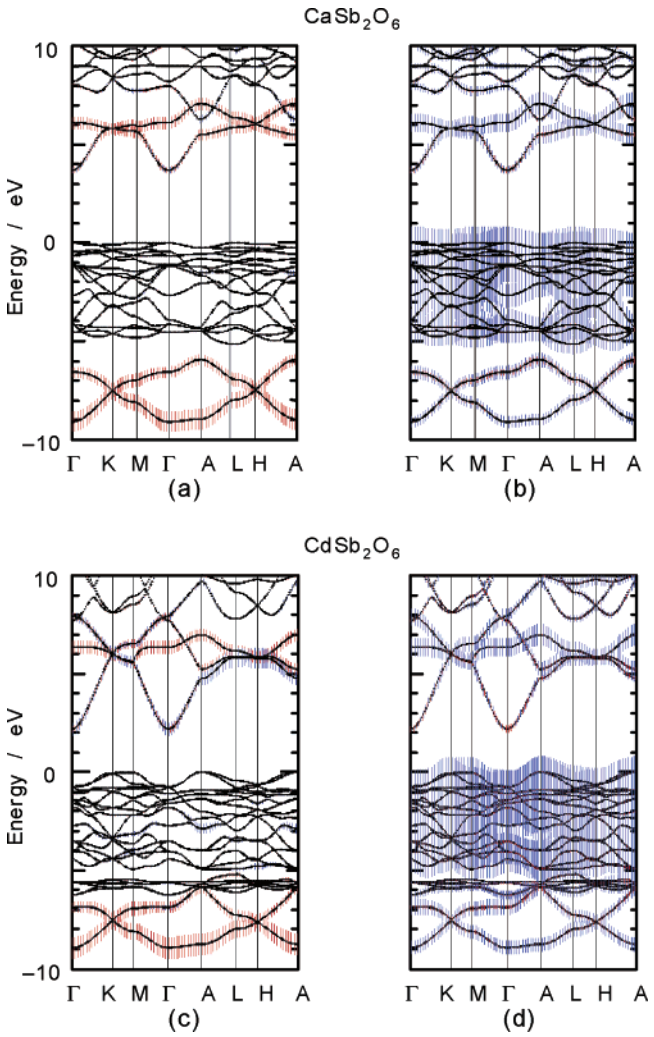

Figure 13. Calculated band structures of $CaSb_2O_6$ (above) and $CdSb_2O_6$ (below). The fatbands on the left-hand side show the Sb 5s orbital contribution in red and the (a) Ca 4s/(c) Cd 5s orbital contribution in blue. The fatbands on the right-hand side show the O 2s orbital contribution in red and the O 2p orbital contribution in blue for (b) $CaSb_2O_6$ and (d) $CdSb_2O_6$.

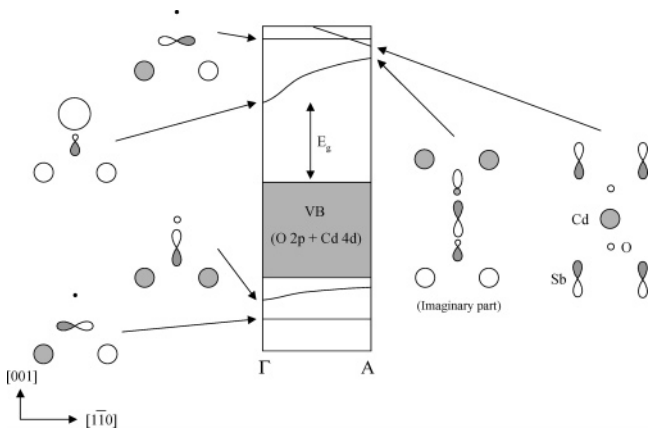

Figure 14. Schematic E vs k diagram for $CdSb_2O_6$ along Γ to A line.

Those with large, electropositive A cations, such as $CaSnO_3$, $NaSbO_3$, $KSbO_3$, and $NaBiO_3$, are essentially layered compounds. These compounds were referred to earlier as stuffed-$PbSb_2O_6$ phases, and it was suggested that they should have electronic structures and properties similar to the compounds with the $PbSb_2O_6$ structure. Inspection of Table 7 shows that this is a good approximation. For example, consider the similarity among the experimentally observed band gaps of $CaSb_2O_6$ (5.0 eV), $SrSb_2O_6$ (5.0 eV), $NaSbO_3$ (4.9 eV), and $KSbO_3$ (4.8 eV). This similarity also extends to the calculated band gaps. A comparable level of agreement exists between $BaBi_2O_6$ and $NaBiO_3$. Consequently, it is not necessary to present the detailed electronic band structures for each of these compounds here, as they are very similar to the band structure of $CaSb_2O_6$ discussed in the preceding section.

When the lower valent A-cation is Ag^+, Zn^{2+}, or Cd^{2+}, the ilmenites are expected to have a three-dimensional electronic structure, due to the covalency of the $A-O$ bonds. Calculated band structures for $CdSnO_3$ and $ZnSnO_3$ are quite similar to that of In_2O_3 ($R\bar{3}c$) (shown in the Supporting Information). As pointed out previously, cadmium and tin are the immediate neighbors of indium in the periodic table. Hence, going from In_2O_3 to $CdSnO_3$ is similar to going from Ge to GaAs, or going from ZnS (zinc blende) to $CuGaS_2$ (chalcopyrite). In the former case, Phillips and Van Vechten showed that the covalent overlap does not change significantly, but the band gap increases due to increased ionicity.[50]

Thus, the relationship between the electronic structures of $CaSnO_3$ and $CdSnO_3$ is very similar to the comparisons already made between $CaSb_2O_6$ and $CdSb_2O_6$ or between $MgSb_2O_6$ and $ZnSb_2O_6$. The introduction of Cd^{2+} as the A-cation creates an inductive effect that (a) increases the CB dispersion, (b) increases carrier mobility, and (c) narrows the band gap. There is one significant difference between ilmenite and the compounds previously discussed. The oxygen in ilmenite is coordinated by four cations in a highly distorted OM_2A_2 tetrahedral unit. Even though the coordination geometry at oxygen is different, a look at the orbital overlap at the CB minimum in corundum In_2O_3 and the ilmenites $ZnSnO_3$, $AgBiO_3$, and $CdSnO_3$ reveal the similarity between these compounds and those previously discussed. The orbital picture at the CB minimum invariably involves all of the cation ns orbitals adding in phase. This effectively prevents mixing with the O 2p orbitals provided the oxygen coordination environment is symmetric.

4. Conclusions

The underlying goal of this work was to identify the compositional and structural features that give rise to an electronic structure favorable for the occurrence of transparent conductivity. The results presented here together with those from an earlier study of perovskites and pyrochlores[9] provide considerable insight to the questions posed in the Introduction. We will now revisit those questions. Before doing so, keep in mind that the focus of this work has been to study the electronic structure and identify characteristics that produce an electronic structure where the lowest energy conduction band is both disperse and split off from the rest of the conduction bands. This is a necessary but not sufficient condition for transparent conductivity. The second condition that must be met in a good TCO material is that it must be possible to effectively dope a compound to introduce carriers and that doping should not seriously degrade the carrier mobility.

Why is octahedral coordination about the cation such a dominant feature, and what is special about ZnO, where the cations are tetrahedrally coordinated? Our results indicate that as far as the electronic structure is concerned, the coordination of the anion, rather than the cation, plays the pivotal role in dictating the dispersion of the conduction band. If the anion coordination environment is symmetric (in terms of the covalent bonding interactions with the surrounding cations) and the cation−anion bonding is reasonably covalent, the conduction band will be disperse. The anion coordination environments in bixbyite In_2O_3 (distorted tetrahedral), corundum In_2O_3 (distorted tetrahedral), SnO_2 (slightly distorted trigonal planar), CdO (octahedral), and ZnO (tetrahedral) are all highly symmetric. Once the importance of anion coordination is understood, it becomes clear that the tetrahedral cation coordination in ZnO is a red herring. The lack of other good examples of TCO materials where the cation is tetrahedrally coordinated can be understood through simple stoichiometry and bonding considerations. If one desires both cation and oxygen coordination environments to be tetrahedral and the stoichiometry to be *M*O, it is necessary to have a main group divalent cation that adopts tetrahedral coordination. There are few cations that meet such criteria. If the covalency is increased by increasing the oxidation state of the cation, a change in stoichiometry occurs. For example, if Zn^{2+} is replaced with Si^{4+}, the stoichiometry changes from ZnO to SiO_2, and the oxygen coordination number changes from four to two. In an MO_2 compound, where *M* is tetrahedrally coordinated, a symmetric environment at oxygen can only be attained as the coordination environment approaches linear. However, there is a strong tendency for small, electronegative, main group ions such as Si^{4+} to favor a bent coordination environment at oxygen. TCO behavior has been observed in compounds containing cations in both tetrahedral and octahedral coordination, such as the inverse spinels, $CdIn_2O_4$ and $MgIn_2O_4$, as well as the aforementioned β-Ga_2O_3. The important point is that these structures possess symmetric anion coordination (distorted tetrahedral in spinel, both distorted tetrahedral and trigonal planar in β-Ga_2O_3).

Is there any reason to favor structures possessing edge-sharing octahedra over those possessing corner-sharing octahedra? In principle, this is not important, but in practice the polyhedral connectivity is closely tied with the anion coordination environment. Since structures based only on corner-sharing octahedra (i.e., ReO_3) are uncommon for main group binary oxides, this question becomes most relevant when considering complex TCOs. A good perspective on this question can be gained by considering the properties of the ilmenite (edge-sharing) and distorted perovskite (corner-sharing) polymorphs of $CdSnO_3$. The measured band gaps of the two polymorphs are very similar (ilmenite = 3.1 eV, perovskite = 3.0 eV[9]) as are the calculated CB widths. Shannon et al. were able to prepare crystals of the perovskite form and introduce oxygen vacancies to obtain conducting samples ($\rho \sim 1$ mΩ cm), whereas attempts to prepare conducting samples of the ilmenite polymorph appear not to have been successful (at least they have not been reported). Thus, there would seem to be no evidence to support the claim that edge-sharing network structures are inherently more likely to produce good TCO materials.

Is TCO behavior limited to compounds where all of the cations have $(n-1)d^{10}ns^0$ configuration, or can electronically inert cations be effectively used in the design of TCO materials? As illustrated previously for CdO, ZnO, In_2O_3, and SnO_2, the anion coordination environment is fairly symmetric in many binary oxides. Upon going to a ternary compound, $A_xM_yO_z$ where *M* is a main group ion, typically the higher valent *M* cations will be asymmetrically arranged around oxygen, and the lower valent *A* cations will complete the coordination sphere. If the covalency of the *A*−O and *M*−O interactions are not too different, as they would be when the *A*-cation has an $(n-1)d^{10}ns^0$ electron configuration, the bonding at oxygen is likely to remain reasonably symmetric and a disperse CB will result. While the CB in such a compound may not be as disperse as a binary oxide, the extra freedom to manipulate the composition and structure allow the possibility to tailor the electronic energy levels in complex TCO materials for application specific needs. On the other hand, if the *A*−O bonding is considerably more ionic than the *M*−O bonding, the electronic environment at oxygen will become asymmetric, and the CB dispersion will tend to be small. Thus, it would seem that in general, the use of electropositive, electronically inert cations is not an effective tool in the search for new complex TCOs. However, before completely discounting this idea, it should be noted that it is possible to introduce electropositive *A*-cations and still maintain a symmetric arrangement of *M*-cations around each oxygen. This is the case in the cubic perovskite $BaSnO_3$ where the oxygen coordination is linear.[9] For reasons we are currently investigating, it appears to be very difficult to dope $BaSnO_3$ at levels that lead to highly conducting samples. Nonetheless, its electronic structure seems almost ideally suited for TCO applications.

Acknowledgment. First we must thank Prof. O. K. Andersen and Dr. O. Jepsen (Max Planck Institute, Stuttgart, Germany) for providing us with the LMTO codes and for support. Dr. H. W. Eng (The Ohio State University) provided valuable guidance and assistance with the calculations as well. We also thank Dr. G. D. Renkes, Dr. N. S. P. Bhuvanesh, Dr. P. W. Barnes, Dr. M. W. Lufaso, Dr. R. L. McCreery, and A. M. Nowak (The Ohio State University) for experimental support. We are grateful for the help of Dr. M. Orita (HOYA Corporation) with understanding the band calculations. Financial support for this research was provided by the National Science Foundation, Grant DMR-0094271.

Supporting Information Available: Six figures of Rietveld refinement results, X-ray diffraction patterns, and calculated band structures for various compounds. This material is available free of charge via the Internet at http://pubs.acs.org.

CM049249W